Structure and Lehmann rotation of drops in a surfactant-doped bent-core liquid crystal

Patrick Oswald, Guilhem Poy, Kanakapura Krishnamurthy

Structure and Lehmann rotation of drops in a surfactant-doped bent-core liquid crystal

Patrick Oswald[1],* Guilhem Poy[2], and Kanakapura S. Krishnamurthy[2]
[1] *Univ Lyon, ENS de Lyon, Univ Claude Bernard, CNRS, Laboratoire de Physique, F-69342 Lyon, France*
[2] *UMR CNRS 5221, Laboratoire Charles Coulomb, Université Montpellier, place Eugène Bataillon, 34095, Montpellier Cedex 5, France*
[3] *Centre for Nano and Soft Matter Sciences, Survey No. 7, Shivanapura, Bangalore 562162, India*

(Dated: July 23, 2022)

The structure of the nematic (cholesteric) drops that form at the clearing temperature of a mixture of the bent-core molecule CB7CB and the rod-like molecule 8CB doped with a surfactant is optically determined. Using experimental observations and numerical simulations, it is demonstrated that the director field inside these drops is not escaped-concentric as previously proposed, but twisted-bipolar. The Lehmann rotation of these drops in the presence of a temperature gradient is described. Their rotation velocity is shown to be proportional to the temperature gradient and to the surface twist angle of the director field and inversely proportional to the drop radius, thus revealing a fundamental scaling law for the Lehmann effect of nematic/cholesteric twisted bipolar droplets.

PACS numbers: 61-30.Eb, 61-30.Dk, 62.25.-g

I. INTRODUCTION

The Lehmann effect is the continuous rotation of liquid crystal drops with a chiral structure subjected to a temperature gradient. Discovered by Otto Lehmann in 1900 [1], this effect was re-observed recently by several authors both in the cholesteric phase of thermotropic liquid crystals (LC) [2–4] and in the nematic phase of a lyotropic chromonic LC when the director field inside the drops is twisted [5]. Although known for a long time, the Lehmann effect still attracts a lot of interest because it is far from being completely understood and because it provides a fundamental model of micro-rotors in the larger context of out-of-equilibrium anisotropic liquids and/or active matter [6]. Several models have been proposed (for a review, see [7]), but none of them is really satisfactory, in particular when the droplets thermodynamically coexist with their own isotropic liquid. In this context, measurements in an additional system are interesting and could help to better understand this effect in the future.

An attractive system for such a study is the nematic phase of the flexible bent-shaped molecule CB7CB (1,7-bis(4-cyanobiphenyl-4-yl)heptane). This molecule is known to give an achiral nematic phase (N) with a giant elastic anisotropy that is responsible for a transition to the nematic twist-bend phase (N_{TB}) with ultrafast dynamics [8] as temperature is lowered. Interestingly, this anisotropy can also be used to prepare drops in which the director field is spontaneously twisted, a necessary condition (but not always sufficient) to observe the Lehmann effect. Such nematic drops were already observed in LC-in-glycerine emulsions [9] and in the coexistence region with the isotropic phase of the LC, first in chromonic liquid crystals [5, 10] and more recently in mixtures of CB7CB and long chain amphiphiles [11]. In the latter study by Krishnamurthy and collaborators, an attentive observation showed that the drops were slowly rotating in the presence of a temperature gradient, revealing a Lehmann effect. This observation was interesting because the Lehmann effect was never observed before in the nematic phase of a thermotropic LC. In addition, the internal structure of the rotating drops was suspected to be escaped-concentric, which was remarkable, as all the drops observed so far in the experiments on the Lehmann effect had other structures.

Motivated by the preliminary study from Krishnamurthy, we characterize here the structures of unconfined droplets and the Lehmann effect in this system, using a combination of experimental and theoretical/numerical approaches.

First, we measured the optical indices and the elastic constants of the LC. These measurements proved to be much more delicate than expected at the transition temperature. Because they are crucial for the rest of this study—especially for the comparison between simulated and experimental microscope images—we detail them in the body of the text and, in particular, present a useful single-sample measurement technique for the elastic constants K_{1-3} (Sec. II). We then present our experimental results on the drops and their rotation in the presence of a temperature gradient—the so-called Lehmann effect—when the LC is doped or not with a chiral molecule (Sec. III). From these measurements, we conclude that the drops are likely twisted bipolar rather than escaped

* patrick.oswald@ens-lyon.fr

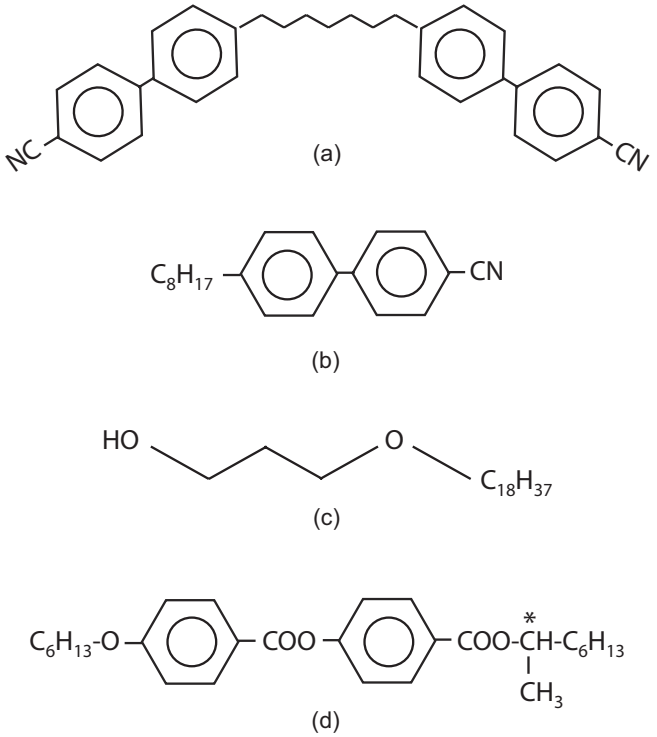

FIG. 1. Molecules used: (a) LC CB7CB; (b) LC 8CB; (c) surfactant OP ; (d) chiral dopant R811.

concentric. To confirm this point, we propose a theoretical study of drops (Sec. IV) in two parts. The first one is devoted to the calculation of their director field by two independent methods—from a generalization of the Williams theory and from a full-vectorial numerical simulation—and the second one is devoted to the calculation of their optical contrast under the microscope thanks to a powerful beam propagation method. Finally, we propose an original experimental scaling law which accounts for all the experimental results on the Lehmann rotation of twisted bipolar droplets (Sec. V). Conclusions and perspectives are drawn in Sec. VI.

II. LIQUID CRYSTAL CHARACTERIZATION

It is well known that the Lehmann rotation velocity of the drops crucially depends on their internal texture. To determine the latter, the elastic constants must be known precisely as well as the birefringence and the spontaneous twist (when the LC is doped with a chiral molecule). These quantities are essential to calculate the director field and then reconstruct the images of the drops under the microscope before comparing them with those actually observed. In this section, we detail these measurements after describing the phase diagram.

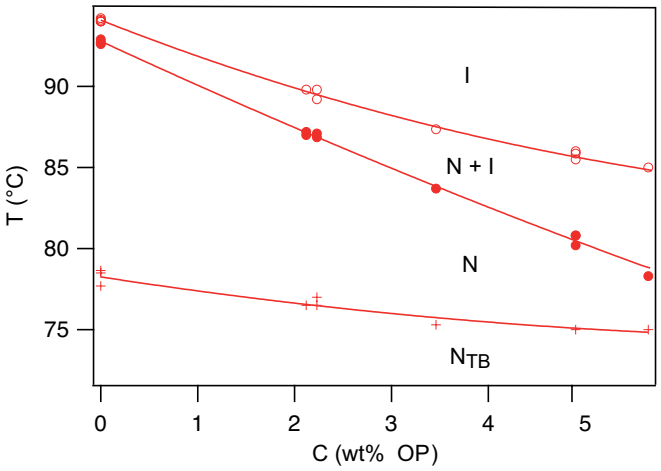

FIG. 2. Phase diagram of the mixture C15 + OP.

A. Phase diagram

The liquid crystal (LC) used is the flexible dimer CB7CB. It was purchased from Synthon (Germany) and used without further purification. It was just dusted off using Pall Nanosep® MF centrifugal devices with a pore diameter of 0.2 µm. All experiments were performed with the lot-No 01422-14680.19. In CB7CB, the spacer between the two cyanobiphenyl (CB) groups contains an odd number of carbons (7) resulting in a bent-shaped molecule [Fig. 1(a)][12]. This molecule is known to be achiral. Because of its shape, this LC has a phase transition between an ordinary nematic and a twist-bend nematic phase at $T_{\mathrm{NB}} \approx 100.4\,^{\circ}\mathrm{C}$. The nematic phase melts at $T_{\mathrm{NI}} \approx 112\,^{\circ}\mathrm{C}$. By mixing CB7CB with a small amount of the rod-like molecule 8CB [4-n-octyl-4'-cyanobiphenyl, Fig. 1(b)], it is possible to substantially decrease both T_{NI} and T_{NB} without increasing too much the domain of existence of the nematic phase. The phase diagram of the mixtures CB7CB+8CB is given in Ref. [13]. For practical reasons (see below), we used the mixture CB7CB+15 wt% 8CB (C15 in the following). The LC 8CB was purchased from Synthon (Germany) and used as received. To further decrease the melting temperature and favor a planar anchoring of the director at the nematic-isotropic interface, C15 was doped with the surfactant 2-octadecoxypropanol (OP). The phase diagram of the mixture C15+OP is shown is shown in Fig. 2. For this measurement and those of birefringence and elastic constants described below, a home-made oven was used to fix the temperature of the samples. The temperature was regulated to within $\pm 0.01\,^{\circ}\mathrm{C}$ thanks to an ATNE ATSR100 PID temperature controller. Inside this oven the temperature is homogeneous to within a hundredth of a degree over the entire surface of the sample (10x10 mm in general). In practice, well-separated spherical drops are observed at large concentration of surfactant, typically more than 5-6% by weight. For this reason, all our measurements on the Lehmann effect

were performed with a mixture C15+5.65 wt% OP. To compensate for a small left-handed chirality of this mixture (see below), this mixture was also doped with very small amounts of the chiral molecule R-(+)-octan-2-yl 4-((4-(hexyloxy)benzoyl)oxy) benzoate [R811 from Merck (Germany), Fig. 1(d)]. We noted that adding R811 did not change in a measurable way the transition temperatures.

B. Optical index measurement

The birefringence was measured using a Berek rotating compensator following the protocol described in Ref. [14]. For this measurement, we prepared planar parallel samples. The glass plates were treated for planar unidirectional anchoring with the polyimide Nissan 0825. 'Parallel' means that the two glass plates were rubbed in the same direction, so that the director is parallel to the glass plates in the middle of the sample in spite of the pretilt angle on the glass plates (of the order of 2°). Nickel wires were used as spacers to fix the sample thickness. The thickness was measured using an USB2000 Ocean Optics spectrometer. Birefringence measurements were performed in the vicinity of the transition temperature, below and above the solidus temperature $T_{\rm NI}$ at which the nematic phase starts to melt. Typical measurements in C15 at three different wavelengths (0.436, 0.546 and 0.633 µm) are shown in Fig. 3(a). These data show that birefringence strongly increases when the temperature decreases below $T_{\rm NI}$ but is almost constant in the coexistence region between the two phases. For this reason, we will use the values of the birefringence measured at the solidus temperature in our optical calculation of the drop images under the microscope (see below). In practice, the drops were observed in mixtures of C15 and the surfactant OP. According to the phase diagram, $T_{\rm NI}$ decreases and the freezing range increases when the concentration of OP increases. So one can expect that the birefringence increases when adding OP, which we checked experimentally by measuring the birefringence at $T_{\rm NI}$ as a function of the concentration of OP. This is shown in Fig. 3(b). Experimentally, the most stable and spherical drops were observed in a mixture C15+5.65 wt% of BP (mixture M1 in the following). At this concentration of OP, the birefringence was difficult to measure because OP starts to precipitate just below $T_{\rm NI}$. For this reason, we found more convenient to extrapolate our birefringence data at this concentration. From the extrapolations shown in Fig. 3(b), we found $\Delta n = 0.0929$ at 0.633 µm, $\Delta n = 0.1011$ at 0.546 µm and $\Delta n = 0.116$ at 0.436 µm. We then fitted these data to a Cauchy law $A + B/\lambda^2 + C/\lambda^4$ to obtain the birefringence at $T_{\rm NI}$ in mixture M1 as a function of the wavelength given in µm:

$$\Delta n \approx 0.06382 + \frac{0.013215}{\lambda^2} - \frac{6.266 \times 10^{-4}}{\lambda^4} \qquad (1)$$

This formula will be used for calculating the image of

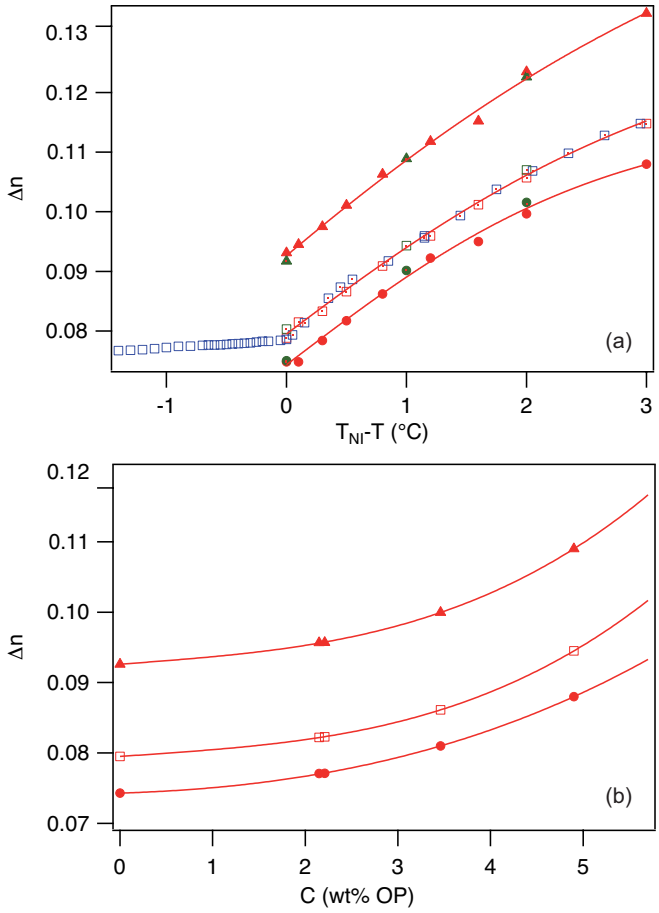

FIG. 3. Birefringence at three different wavelengths: 0.436 µm (filled triangles), 0.546 µm (empty squares), 0.633 µm (filled circles). (a) Variation as a function of temperature. The three different colors correspond to three different samples. (b) Values measured at $T_{\rm NI}$ as a function of the concentration of OP. Solid lines are the best fits with a third-order polynomial.

drops under a microscope. For this purpose, we also need to know the optical index n_i of the isotropic liquid and the ordinary index n_o in the nematic phase. We measured n_i above the solidus temperature in the mixture M1 using the wedge cell technique [15]. A wedge cell was prepared between two ITO glass plates of low resistivity. The angle of the wedge was set with a gold wire of diameter 50 µm. Under a microscope with a low power (4×) objective and monochromatic illumination, succession of interference fringes was observed. From the interfringe distances $i_{\rm air}$ and $i_{\rm LC}$ measured before and after the cell was filled with the LC, we deduced the index $n_i = i_{\rm air}/i_{\rm LC}$. In practice, the fringes were visible under the microscope at 0.633 µm and 0.546 µm, but were not detectable at 0.436 µm. Our measurements at the first two wavelengths are shown in Fig. 4. From these measurements as a function of temperature above the liquidus temperature, we extrapolated the value of the index of the isotropic phase in the middle of the coexistence region, at about 81.5°C, which is

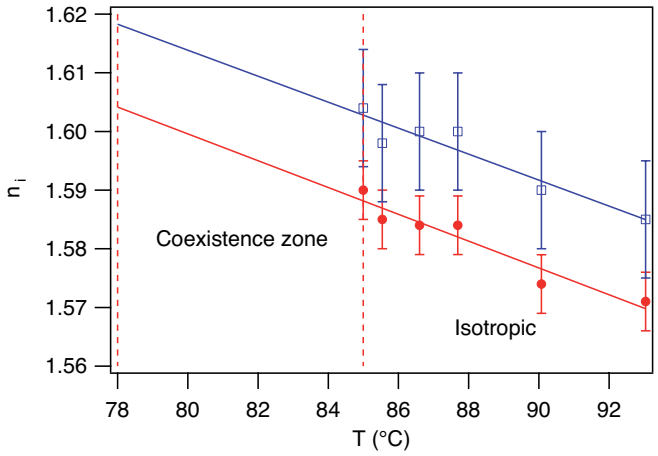

FIG. 4. Optical index n_i of the isotropic liquid as a function of temperature in mixture M1 at two wavelengths: 0.633 µm (filled circles) and 0.546 µm (empty squares). The solid lines represent the best linear fit to the data. The two vertical dashed lines mark the solidus and liquidus temperatures.

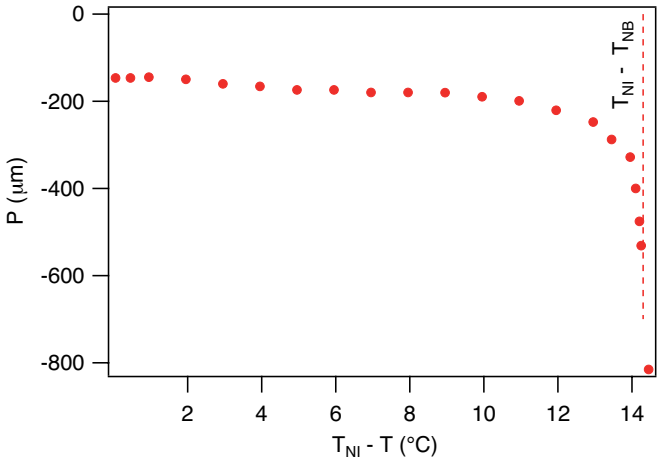

FIG. 5. Pitch as a function of temperature in the mixture C15. The pitch is negative, meaning that we are in reality dealing with a long-pitch left-handed cholesteric phase.

the temperature at which the drops were usually observed in the mixture M1. This gave $n_i(0.546\,\mu\text{m}) \approx 1.61$ and $n_i(0.633\,\mu\text{m}) \approx 1.597$. The value of the index at the other wavelengths was calculated by using a simplified Cauchy law $n_i = A_i + B_i/\lambda^2$. From the two values found at 0.633 µm and 0.546 µm, we calculated

$$n_i \approx 1.5592 + \frac{0.015139}{\lambda^2}, \tag{2}$$

where λ is in µm. This yields $n_i(0.436\,\mu\text{m}) = 1.648$.

Finally, we deduced the values of the ordinary index n_o and extraordinary index n_e by assuming that $n_o = n_i - \Delta n/3$ and $n_e = n_i + 2\Delta n/3$. These relations are known to give n_e and n_o at the transition temperature with a typical error less than 1 % [16]. By using the two previous relations (1) and (2), we found

$$n_o \approx 1.538 + \frac{0.010734}{\lambda^2} + \frac{2.089 \times 10^{-4}}{\lambda^4}, \tag{3}$$

$$n_e \approx 1.602 + \frac{0.023949}{\lambda^2} + \frac{4.178 \times 10^{-4}}{\lambda^4}. \tag{4}$$

C. Pitch measurement

In principle, 8CB, CB7CB and OP are not chiral materials, so one expected to observe a nematic phase below T_{NI} in C15 and its mixtures with OP. In practice, the situation turned out to be different as we noted immediately by observing that the drops were all rotating in the same direction in the coexistence region of the mixture C15+5.65wt% OP in the presence of a vertical gradient. This clearly indicated that the director field was twisted in the same direction in all drops, showing the existence of a chiral bias in our samples. For this reason, we systematically measured the pitch in mixtures of C15 for different concentrations of OP and found it was essentially the same in all the mixtures studied, ranging between −150 µm and −140 µm. This clearly indicated that OP was not chiral. We then measured the pitch in the pure mixture C15 and found the same pitch, showing that either CB7CB or 8CB was chiral. After checking that our 8CB was not chiral, we concluded that our lot of CB7CB contained a chiral impurity.

In practice, the classical Cano wedge technique [17] could not be used to measure the pitch because it was too large. For this reason, we chose another method consisting of measuring the rotatory power of thin samples sandwiched between a plate treated for planar unidirectional anchoring and a second one treated for planar sliding anchoring. The details of this technique are given in Ref. [14]. In short, the sample was placed under the microscope and was illuminated with a polarized monochromatic light beam whose incident polarization was parallel to the director on the bottom plate treated for planar unidirectional anchoring. The rotatory power was determined by measuring for which angle between the polarizer and the analyzer the transmitted intensity I_{tr} was maximum. From this angle, the pitch was determined by using the Ong formula [18, 19] that allowed us to calculate I_{tr} knowing the birefringence at the wavelength chosen (in our measurements, 0.546 µm). Note that using this formula was necessary when T was close to T_{NI}, because the Mauguin condition for the adiabatic rotation of the light polarization was not fully satisfied under these conditions.

A curve of pitch vs. temperature for the mixture C15 is shown in Fig. 5. As expected, the pitch is almost constant at high temperature (close to −145 µm at T_{NI}) and it strongly increases (in absolute value) – without diverging– upon approaching the N_{TB} phase. This result agrees with previous measurements in the vicinity of the N_{TB} phase [20, 21].

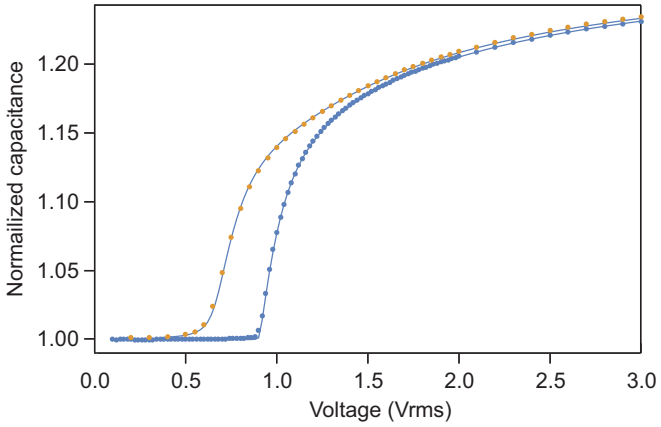

FIG. 6. Normalized capacitance curves obtained with the same planar parallel sample of CB7CB+2.25 wt% OP at 86.5°C ($T_{NI} - T = 0.4$°C). Data in blue have been obtained by increasing the voltage and those in yellow by decreasing the voltage. $d = 17.1\mu$m, $\theta_a = 2°$, $\alpha = 0.283$, $K_1 = 1.8$ pN, $K_2 = 0.85$ pN, $K_3 = 0.576$ pN, $P = -145$ µm.

In addition, we measured the helical twist power (HTP) of the chiral molecule R811 in C15. The measurement was made by using the classical Cano wedge technique with a sample of C15 doped with 1 wt% of R811. It gave HTP=19 μm^{-1} $wt\%^{-1}$ at the transition temperature. From this measurement, the concentration of R811 required to compensate our samples was evaluated to be about 0.036 wt%. Hence forward, we refer to the nearly compensated mixture, M1+0.036 wt% R811, as M2.

D. Elastic constants measurement

Measuring precisely the elastic constants is essential to determine the director field inside the drops.

In principle, the elastic constants can be obtained from capacitance measurements of planar samples. In general, two types of cells are used: antiparallel planar cells to determine the splay and bend constants K_1 and K_3 and $\pi/2$-twisted cells to determine the twist constant K_2 knowing K_1 and K_3. Apart from the fact that it is necessary to prepare two types of cells, the main disadvantage of this method is that one can never be completely sure that the constants are measured exactly at the same temperature. This becomes a serious problem when measurements are made in the vicinity of the melting temperature T_{NI} because the elastic constants change rapidly with temperature in this region. In addition, the larger the concentration of OP, the larger would be the uncertainty in T_{NI}. This can cause significant errors in samples with a high concentration of OP. For these reasons, we looked for an alternative method allowing us to measure the three constants simultaneously in the same cell (and consequently exactly at the same temperature with respect to T_{NI}).

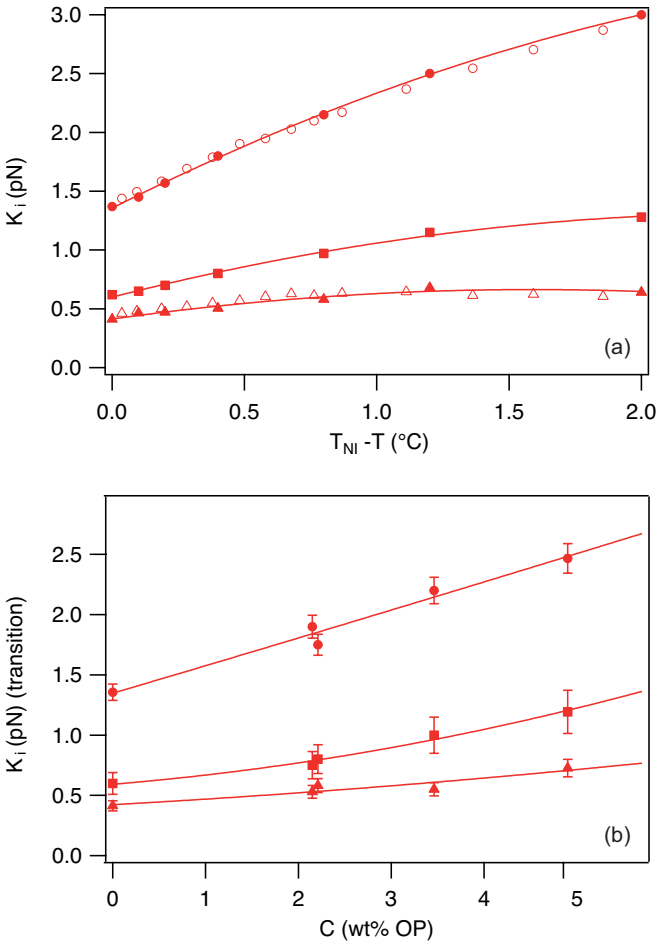

FIG. 7. (a) Elastic constants as a function of temperature in C15. Filled and empty symbols correspond to two different samples. (b) Elastic constants measured at T_{NI} as a function of the concentration of OP. In the two graphs, the circles correspond to K_1, the squares to K_2 and the triangles to K_3. The solid lines show the best fits with a fourth-order polynomial. These fits give $K_1 = 2.67$ pN, $K_2 = 1.36$ pN and $K_3 = 0.77$ pN at $C = 5.65$ wt%.

For this purpose, we used planar parallel cells of typical thickness 22 μm. The two ITO electrodes were treated with the polyimide Nissan 0825 and rubbed in a single direction to induce a planar unidirectional anchoring. The pretilt angle θ_a was close to 2° (see Appendix A). The protocol was the following. First, we measured the capacitance curve of the sample between 0.1 and 3 Vrms when the director field inside was not twisted (this is the case when the sample is cooled from the isotropic phase). In practice, measurements were taken with a LCR meter HP 4284A controlled with a LabView program by using increments of 0.01 Vrms between 0.1 and 2 Vrms and of 0.1 V between 2 and 3 Vrms and time interval between each measurement of 20 s. Note that a little over an hour is needed to record a full capacitance curve. From the fit of this curve we obtained K_1 and K_3 (see Appendix A). We then imposed a large electric field to form

a π-wall [22] (in practice a voltage of 20 Vrms was always sufficient near $T_{\rm NI}$). In all our samples, this wall formed after propagation on one plate of a $+1/2$ surface disclination line [23] and not via a biaxial melting of the nematic order in the midplane as described in Ref. [24]. Once the wall was formed, the voltage was switched to 3 Vrms, resulting in a director field twisted by 180°, and a new capacitance curve was obtained by slowly decreasing the voltage down to 0.1 V by increments of -0.05 V. In that case, the curve was recorded manually to minimize the measurement time while being sure that the sample was equilibrated after each voltage change. In this way, it only took 10 to 15 minutes to record the capacitance curve. This precaution was taken to prevent the sample from reorienting during the measurement, which could happen if the measurement time was too long. From the fit of this new curve, the constant K_2 was deduced since both K1 and K3 were known from the analysis of the previous curve. An example of capacitance data obtained this way is shown in Fig. 6 with the corresponding fits. In this graph the normalized capacitance is the capacitance divided by the capacitance measured at very low voltage below the onset of instability. The equations and the protocol used to fit the two capacitance curves are recalled in Appendix A. The elastic constants measured for C15 are shown in Fig. 7(a). From similar measurements in mixtures of C15 and OP we deduced the values at $T_{\rm NI}$ of the elastic constants for different concentrations of OP. The result is shown in Fig. 7(b). Note that we did not measure the elastic constants in the mixture C15+5.65 wt% OP, because OP tends to precipitate and form small aggregates at $T_{\rm NI}$ in this mixture. This phenomenon was also observed in the other mixtures, but at a temperature lower than T_{NI}.

III. DROPS AND LEHMANN EFFECT: EXPERIMENTAL RESULTS

A. Drop observation

All observations were made with a Leica Laborlux 12 Pol Microscope equipped with a Leitz NPL FLUOTAR L 25 objective of numerical aperture 0.35 and a Guppy F-503 CMOS camera. The aperture diaphragm of the microscope was closed to the maximum resulting in a numerical aperture of the illuminating beam of the order of 0.05. All observations were made in white light produced by a 100 W halogen lamp, whose spectrum was measured with our spectrometer. A Mettler oven FP85 was used to observe the drops in the coexistence region. The samples were prepared between Duran soda lime float glass slides of thickness 1 mm and optical index 1.51. A thin film of a polymercaptan was deposited by spin-coating on the plates following the protocol described in Ref. [25]. The sample thickness was fixed with Nickel wires and was close to 22.5 μm in all our experiments with the drops.

The first observations of drops were made in the mix-

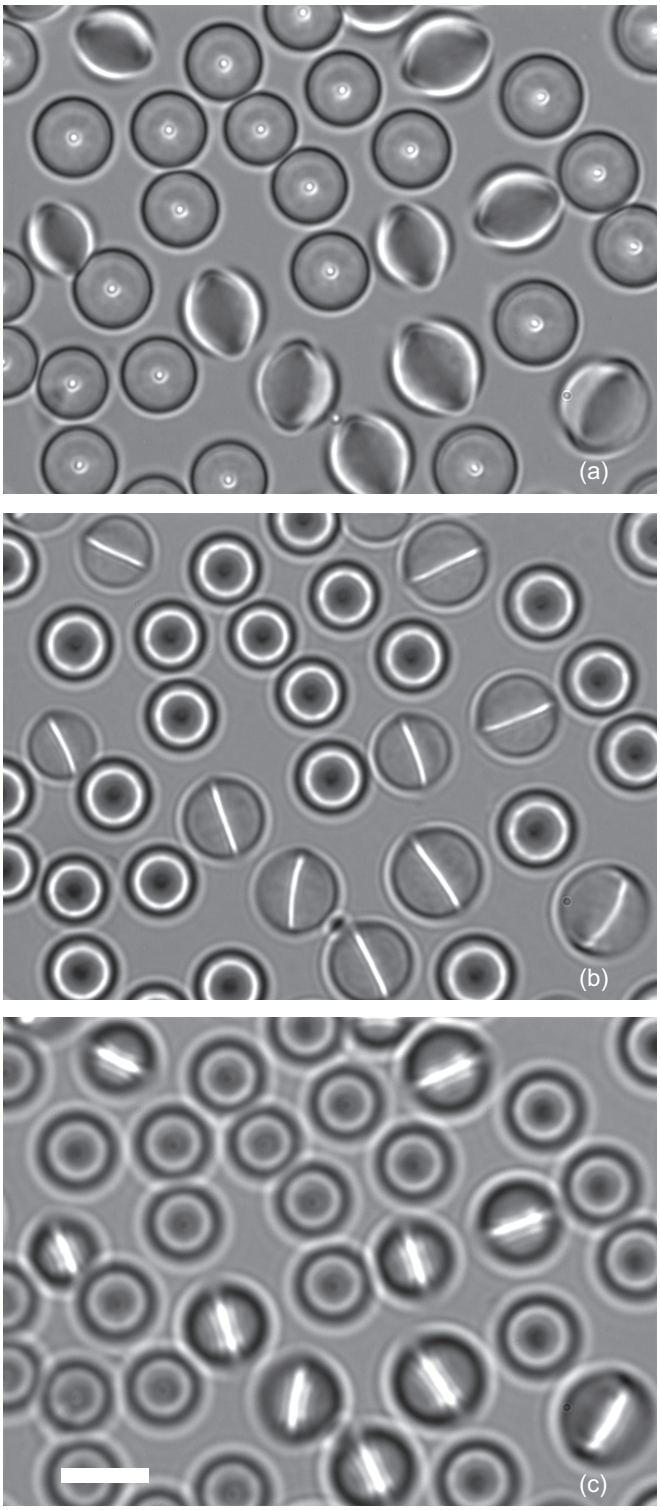

FIG. 8. Texture of nematic drops coexisting with the isotropic phase in the mixture M1 at 81.5°C. Observations in unpolarized white light at focusing distances $z = -16\,\mu$m (a), 0 (focus on the bright band) (b) and 17 µm. Mixture M1, $T = 81.5$°C. The white bar is 20 µm long.

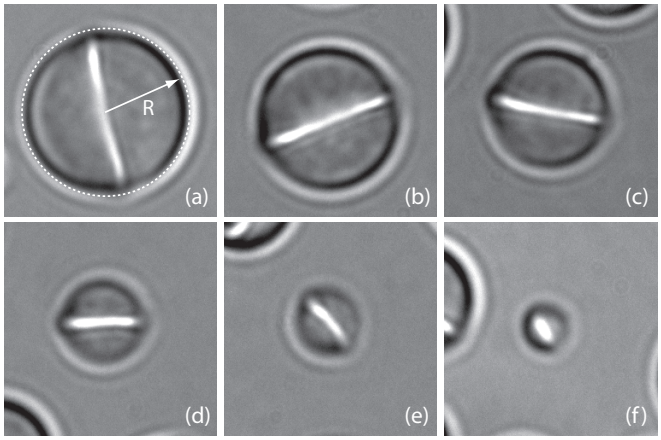

FIG. 9. Observation of drops of different radii in unpolarized white light. The bright band is visible in all of them, whatever their size. The definition of the drop radius R is shown on the first image. From (a) to (f), $R = 11.2, 10.2, 8.6, 6.1, 5.1$ and $3.5\,\mu$m. Mixture M1, $T = 81.5°$C

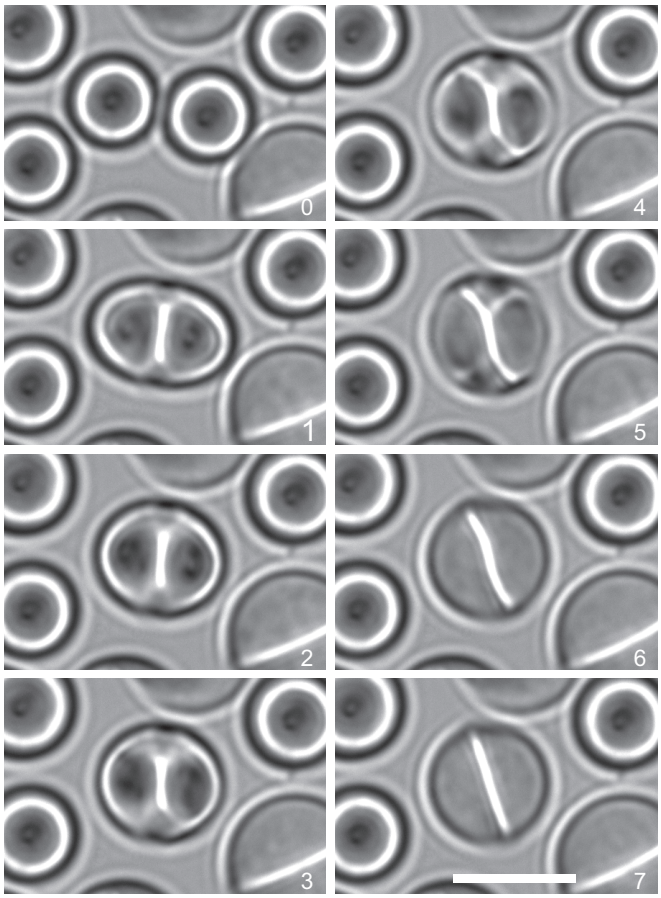

FIG. 10. The coalescence of two drops oriented vertically gives a drop oriented horizontally. The time is indicated in second on the images. The white bar is $20\,\mu$m long.

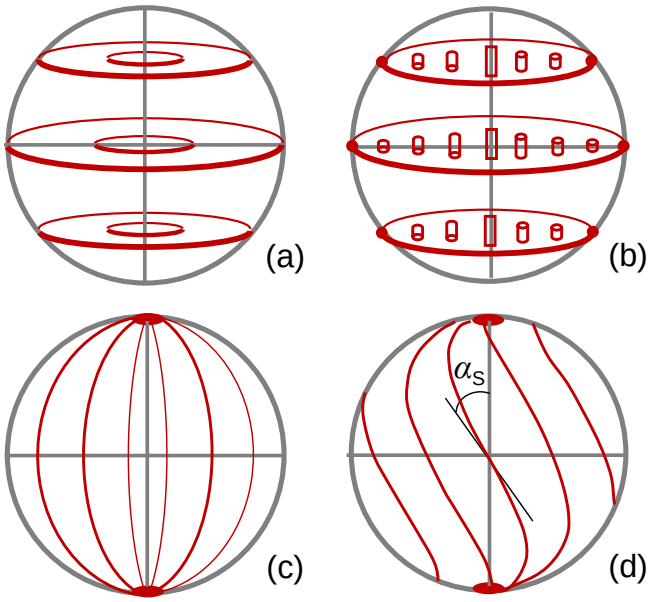

FIG. 11. The four possible configurations; (a) Ideal concentric (C) configuration; (b) Escaped concentric (EC) configuration; (c) Bipolar (B) configuration; (d) Twisted bipolar (TB) configuration. Angle α_S is the twist angle at the drop surface.

ture M1 (C15+5.65 wt% OP). By decreasing the temperature from the isotropic phase to the coexistence zone, we observed the nucleation and growth of drops similar to those described in Ref. [11]. Two different textures corresponding to the same drops oriented with their revolution axis either parallel or perpendicular to the plates are usually observed and are shown in Fig. 8. The photo Fig. 8(b) was taken under white light without polarizers by focusing on the thin bright band that forms under the microscope when the drop axis is horizontal. The other two photos Fig. 8(a) and Fig. 8(c) were taken at the same location by defocusing by $16\,\mu$m down and by $17\,\mu$m up, showing that the drop contrast crucially depends on the focus, a point that we will explore further in the next section. The bright band is visible in all the horizontal droplets, whatever their radius, as can be seen in Fig. 9. We noted that the vast majority of drops were oriented vertically when they nucleated. They were then very small. By decreasing the temperature, they grew and coalesced when they touched each other, as shown in Fig. 10 and Supplementary Movie SM1 [26]. During this process, they systematically changed orientation and formed bigger droplets with their axes of revolution horizontal.

In the literature, this band was often interpreted as due to the presence of a +1 disclination line along the drop axis. Two models are possible in that case: either the line is singular and the droplet has the ideal concentric (C) configuration (also called toroidal configuration [27]) or the line escapes in the third dimension leading to a twisted non singular configuration in the bulk, the so-called escaped concentric (EC) configuration [9, 28].

Two other configurations are possible when the director is planar at the drop surface: the bipolar (B) configuration in which the director field is not twisted and the twisted bipolar (TB) configuration in which the director field is radially twisted by an angle α_S at the drop surface different from 0 (the limit $\alpha_S = \pi/2$ identifying with the previous EC configuration). The four configurations are represented in Fig. 11.

At this level, it is difficult to know what is the actual configuration. Further investigations are therefore necessary. First, we observed carefully the drops under the microscope over long periods of time. While doing this, we observed that all the drops with a bright band inside were slowly rotating inside the oven, revealing the Lehmann effect already reported in Ref. [11] (Fig. 12). This rotation was caused by the presence of a very small vertical temperature gradient directed upwards in the oven. For symmetry reason, the drop rotation is only possible if the director field is twisted, allowing us to immediately exclude the models C and B [Fig. 11(a) and (c)]. Moreover, consistently with our observation above that C15 had a chiral character, we saw that all droplets featured a counter-clockwise rotation, i.e., they were all twisted with the same handedness. This result was confirmed by measuring the pitch of our mixtures which turned out to be negative (left-handed cholesteric) and close to $-145\,\mu m$ at T_{NI} (see above). This confirmed that our batch of CB7CB contained a chiral impurity. The reader will note that the sense of rotation observed in this experiment is compatible with all the previous observations on the Lehmann effect, namely that the rotation vector and the temperature gradient are of the same sign when the pitch is negative [7]. Finally, we noticed that the horizontal droplets systematically tended to reorient themselves vertically after a certain period of time. This process of reorientation is shown in Fig. 13 and Supplementary Movie SM2 [29]. The consequence was that after a few hours all the drops were oriented vertically in the sample.

B. Lehmann rotation

To check whether it was possible to suppress the chiral bias, we compensated our mixture by adding 0.036 wt% of the chiral molecule R811 and we measured the pitch of this new mixture M2: as expected, we found it was very large, close to -2 mm. With this mixture we observed that most of the horizontal droplets were still rotating CCW except for a few of them that were rotating CW (see Supplementary Movie SM3 [30]), revealing there was still a small chiral bias compatible with our pitch measurement. We also observed that the rotation velocity was almost the same as in the previous mixture M1 in absolute value. In other words, the droplets were still rotating at the compensation point, meaning that the director field was still twisted in the drops in the compensated nematic-like phase. We also prepared two other mixtures, M3 and M4 by adding larger concentrations of R811 to M1. For M3, we measured $P \approx 167\,\mu m$ and for M4, $P \approx 44\,\mu m$. In these two mixtures, the droplets were all rotating CW in the oven, as expected since the pitch is now positive. On the other hand, we found that their velocity at similar radius was similar to that found in the two other mixtures. This observation was at first sight compatible with the EC configuration insofar as in this configuration all the drops are twisted in the same way.

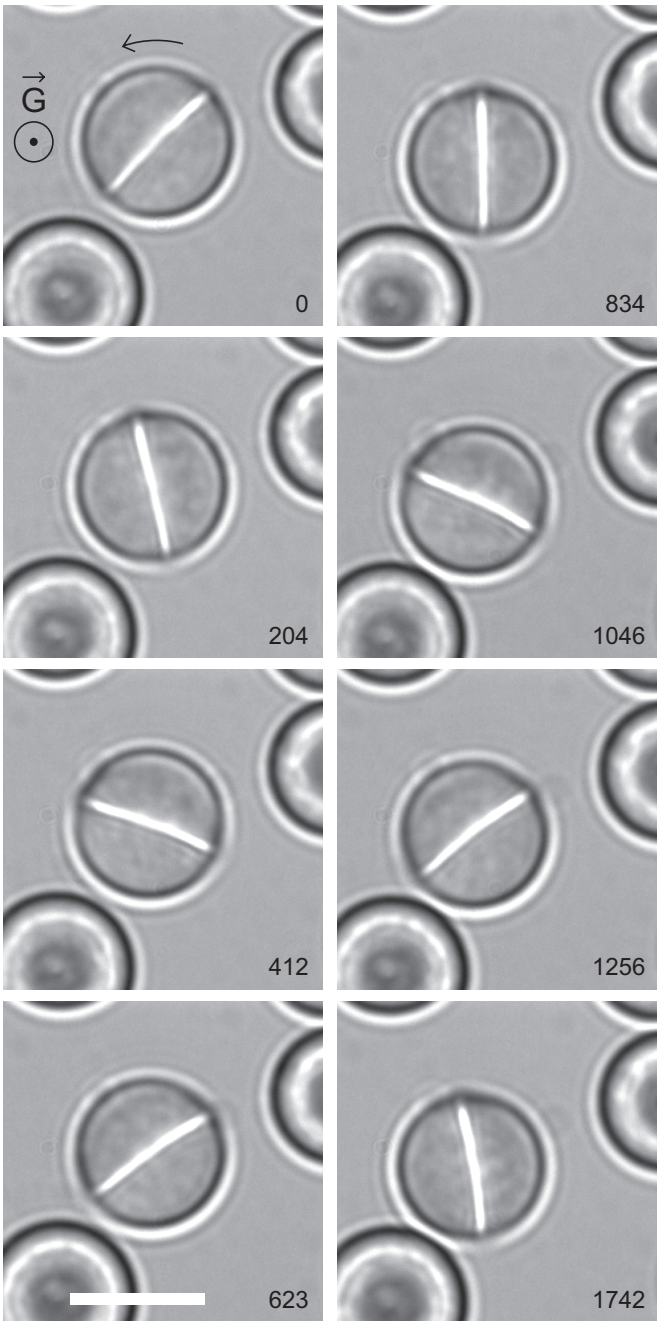

FIG. 12. Lehmann rotation of a drop with its axis of revolution horizontal observed in the Mettler oven. The time is indicated in second on each photo. The bright band is rotating counter-clockwise and the temperature gradient is directed upwards. The white scale bar is 20 µm long.

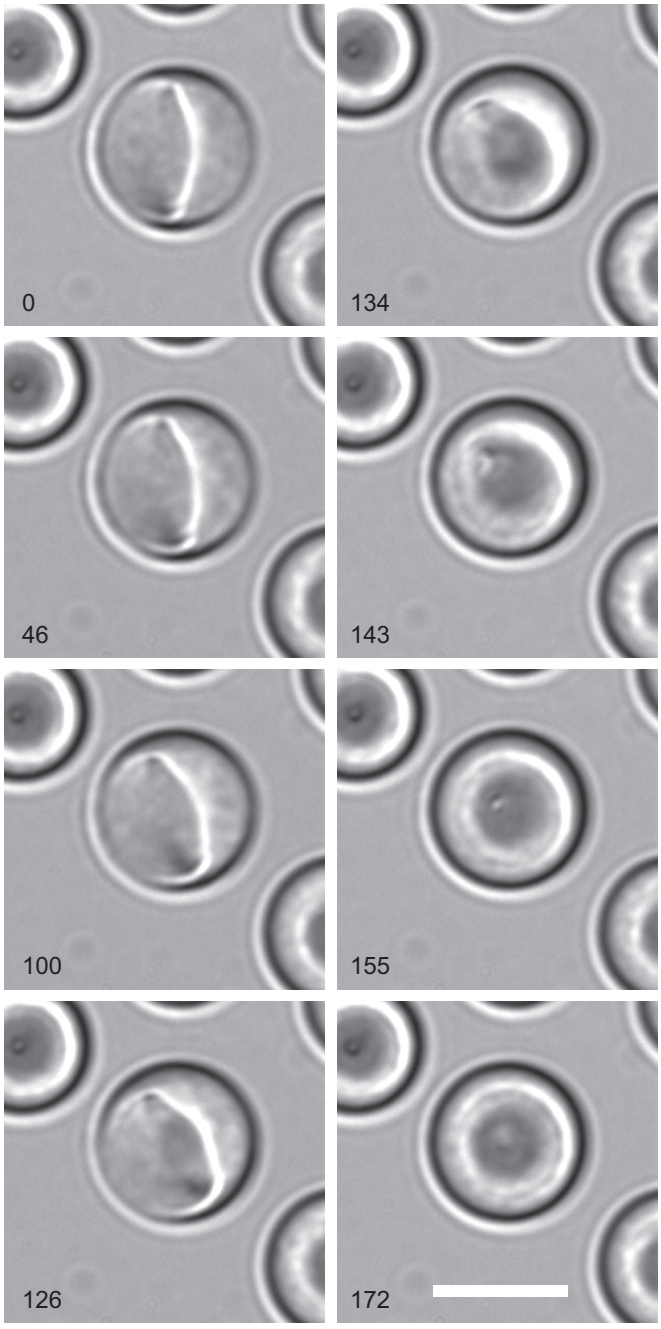

FIG. 13. Spontaneous reorientation of a drop in the Mettler oven. The time is indicated in second on the photos. The bright band on the photo at $t = 0$ is slightly curved, meaning the droplet axis is already slightly tilted with respect to the horizontal plane. The white scale bar is 20 µm long.

Another possibility would be that we are dealing with droplets in the TB configuration in which the twist angle is mainly fixed by the elastic anisotropy and depends very little on the actual pitch of the phase (this point will be discussed in the next Section). In this second case, we should nonetheless observe differences between the mixtures M1-M4.

To check this point, we thus performed precise systematic measurements of the drop rotation velocity in the four mixtures M1-M4. To this end, we modified our vertical temperature gradient setup already described in Ref. [2] by replacing the water-circulating top oven by a conventional oven equipped with a sapphire window to minimize the horizontal temperature gradients. In this way, it was possible to work at higher temperatures than with our previous setup. With this new system the temperature of the top oven can now be increased well above 100°C and is regulated within ±0.01°C thanks to a RKC HA400 controller, while the temperature of the bottom oven is regulated within ±0.01°C with a water circulating bath and so cannot exceed 85°C typically. This limitation explains why we doped our CB7CB with 15 wt % 8CB to decrease the melting temperature.

To measure the rotation velocity of the drops, we placed our samples between the two ovens. The samples were sealed on the sides with NO81 UV glue. A thin layer of glycerine ensured good thermal contact between the ovens and the samples. We measured the period of rotation Θ of the drops in the four mixtures as a function of the their radius R. In practice, measurements were only possible at low temperature gradient, when the temperature difference ΔT between the top and bottom ovens did not exceed 6°C. At larger ΔT, the nucleation rate of new drops was so high that it became impossible to perform reliable measurements. We also limited our measurements to droplets of diameters smaller than the sample thickness (22.5 µm) and larger than 7 µm, as small droplets were very unstable, changing radius or reorienting vertically too fast to allow us to measure precisely their rotation velocity. In mixture M1, we measured the rotation velocities at two temperature gradients by taking $\Delta T = 3$ and 6°C, while in the other mixtures all measurements were performed by taking $\Delta T = 3$°C. The temperature gradient inside the liquid crystal is approximately given by $G(\mathrm{K/mm}) \approx 7\Delta T/3$ by assuming that the thermal conductivity ratio $\kappa_{\mathrm{glass}}/\kappa_{\mathrm{LC}} \sim 7$ as in usual cyanobiphenyls [2]. Our results are reported in Fig. 14. The first graph measured with the mixture M1 shows that the drop rotation velocity is proportional to the temperature gradient, as in all earlier experiments on the Lehmann effect [7]. The second graph measured with the almost compensated mixture M2 shows that the period of rotation period is proportional to the drop radius. This linear law was already observed in the nematic phase of a chromonic LC in which the droplets had a TB structure [5] with a twist angle at the surface of the drop close to 70°. By contrast, this linear law fails for all the other mixtures in which the pitch has a finite value. This is the case in mixtures M1, M3 and M4 for which the data are well fitted with a parabolic law. Note that the rotation velocities are almost identical (in absolute value) in the two mixtures M1 and M3, which is expected because the pitches measured in these two mixtures are quite close in absolute value. These measurements show that the existence of a spontaneous

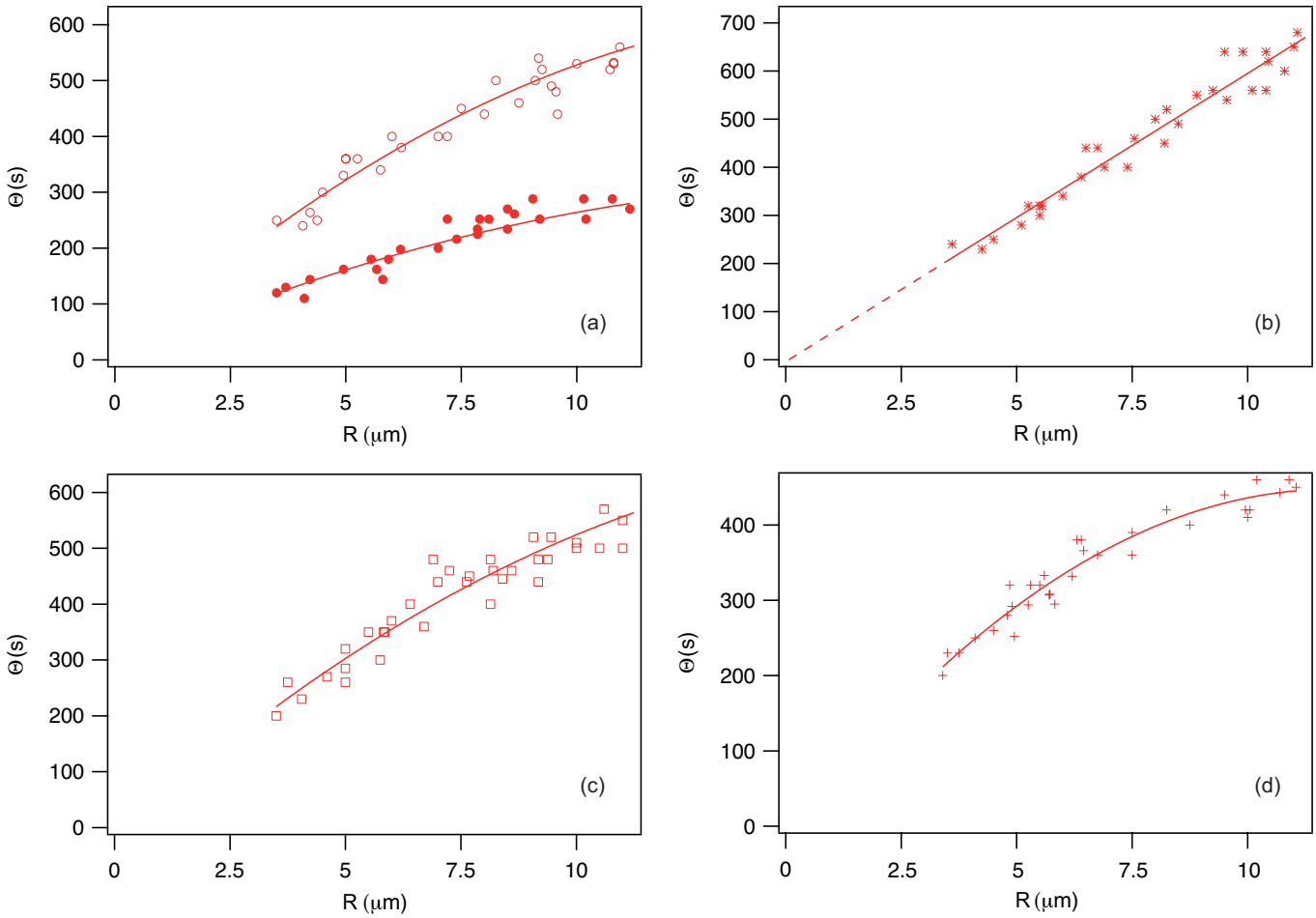

FIG. 14. Period of rotation Θ of the drops as a function of their radius R. (a) Mixture M1, $\circ$: $\Delta T = 3°$C, $\bullet$: $\Delta T = 6°$C. The two solid lines correspond to a global fit with two parabolas by assuming that Θ is proportional to ΔT; (b) Mixture M2, $\star$: $\Delta T = 3°$C. The solid line is the best fit with a straight line; (c) Mixture M3, $\square$: $\Delta T = 3°$C. The solid line is the best fit with a parabola; (d) Mixture M4, $+$: $\Delta T = 3°$C. The solid line is the best fit with a parabola.

twist changes slightly –but measurably– the value of the rotation velocity. More precisely, the larger the pitch (in absolute value), the larger is the period of rotation or the smaller is the rotation velocity. Such a dependency was already observed in the LC CCN37 which featured TB droplets when the LC was doped with a chiral impurity [31].

These results strongly suggest that our droplets are twisted bipolar with a twist angle at the drop surface that weakly depends on the pitch –and not escaped concentric as proposed before– because, in that case, all droplets should rotate in a similar way in the four mixtures. To test this conclusion, we calculated the director field inside the drops by using the values of the elastic constants measured experimentally and we then computed the corresponding drop images to compare them with the experimental images.

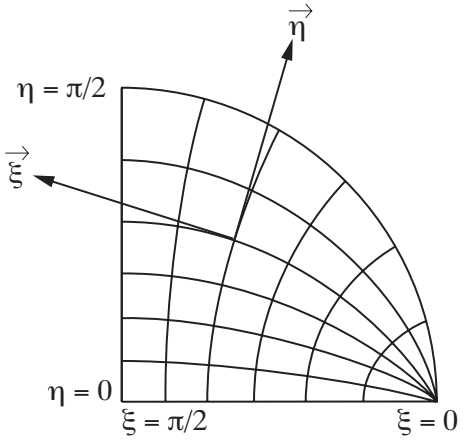

FIG. 15. Bispherical coordinate system with unit vectors used by Williams. The vector $\vec{\theta}$ is normal to the paper (from Ref. [32]).

IV. DIRECTOR FIELD IN THE DROPS: THEORETICAL RESULTS

To calculate the director field inside the drops, we first generalized to cholesterics the Williams theory for tangentially anchored nematic droplets [32]. From this calculation, the twist angle at the surface of the drop was calculated as a function of the cholesteric pitch by using Mathematica. Because this calculation is not exact and relies on a simplified ansatz for the director field, we also extracted this angle from a full-vectorial numerical calculation of the director field. This allowed us to test the accuracy of the Williams model.

A. Williams prediction

To calculate the director field inside bipolar droplets, Williams proposed to use bispherical coordinates (ξ, η, θ) [32] (Fig. 15). In this system, θ is the polar angle in cylindrical coordinates (z, r, θ) where the z-axis passing through the poles. The lines of constant η are circles passing through both poles, while the orthogonal set of constant ξ are also circles. For calculating the director field, Williams assumed that the director $\vec{n}$ has no $\vec{\eta}$ component and wrote

$$\vec{n} = \vec{\xi}\cos[\alpha(\eta)] + \vec{\theta}\sin[\alpha(\eta)], \tag{5}$$

where $\vec{\xi}$, $\vec{\eta}$ and $\vec{\theta}$ is the triad of unit vectors and α the twist angle. By using this ansatz, Williams calculated the Frank elastic energy and minimized it to obtain the Euler-Lagrange equation that $\alpha(\eta)$ must satisfy. Redoing this calculation but taking into account the spontaneous twist $q = 2\pi/P$ in the Frank energy we found

$$\begin{aligned} 4K_{21}\left(\eta\frac{\mathrm{d}^2\alpha}{\mathrm{d}\eta^2} + \frac{\mathrm{d}\alpha}{\mathrm{d}\eta}\right) &= \sin(2\alpha)[(4 - 2K_{21} + 3K_{31})\cot\eta + (-4 + 2K_{21} + K_{31})\eta\,\mathrm{cosec}^2\eta + 2\eta\cot^2\eta(K_{21} - 2K_{31}\cos^2\alpha] \\ &\quad - qR\left[\mathrm{cosec}\,\eta\,(\eta + 2\cot\eta - 2\eta\,\mathrm{cosec}^2\eta) + (1 - \eta\cot\eta)\cot\eta\,\mathrm{cosec}\,\eta\cos(2\alpha)\right]. \end{aligned} \tag{6}$$

where $K_{21} = K_2/K_1$ and $K_{31} = K_3/K_1$ are the elastic anisotropies and R is the drop radius. We emphasize that Williams showed that the Gauss (or saddle-splay) term contributes to a constant term in the free energy of the droplet [32], which is why the associated elastic constant do not appear in the previous equation. We also note that although the free energy density diverges near the polar defects, the total free energy is always integrable and finite for the ansatz used by Williams. This can be directly checked numerically by defining a cutoff integration radius around the defects and looking at the energy limit when this cutoff goes to zero.

This equation must be solved with the boundary conditions

$$\alpha(0) = 0 \tag{7}$$

which ensures that the director field is not singular on the pole axis and

$$\alpha'(\pi/2) = 2qR/\pi \tag{8}$$

where $\alpha' = \mathrm{d}\alpha/\mathrm{d}\eta$, which is the torque equation at the drop surface for a sliding planar anchoring.

The droplet energy in units of K_1R is given by $E = E_1 + K_{21}E_2 + K_{31}E_3$ where E_1, E_2 and E_3 are the splay, twist and bend energies given by

$$E_1 = 4\pi\int_0^{\pi/2}\frac{\mathrm{d}\eta}{\sin^2\eta}(\eta - \cos\eta\sin\eta)\cos^2\eta, \tag{9}$$

$$\begin{aligned} E_2 &= 2\pi\int_0^{\pi/2}\mathrm{d}\eta\,\eta(\alpha' + \sin\alpha\cos\alpha\cot\eta) \\ &\quad + 4\pi\int_0^{\pi/2}\mathrm{d}\eta\,(\eta\cot\eta - 1)\mathrm{cosec}\,\eta(\alpha' + \cot\eta\cos\alpha\sin\alpha)qR \\ &\quad + (4 - \pi)\pi q^2R^2, \end{aligned} \tag{10}$$

$$E_3 = \pi\int_0^{\pi/2}\mathrm{d}\eta\left[\frac{\eta}{\sin^2\eta}(1 + \sin^2\alpha + 2\cos^2\eta\cos^4\alpha) - 3\cot\eta\cos^2\alpha\right]. \tag{11}$$

These formulas generalize those of Williams to cholesterics.

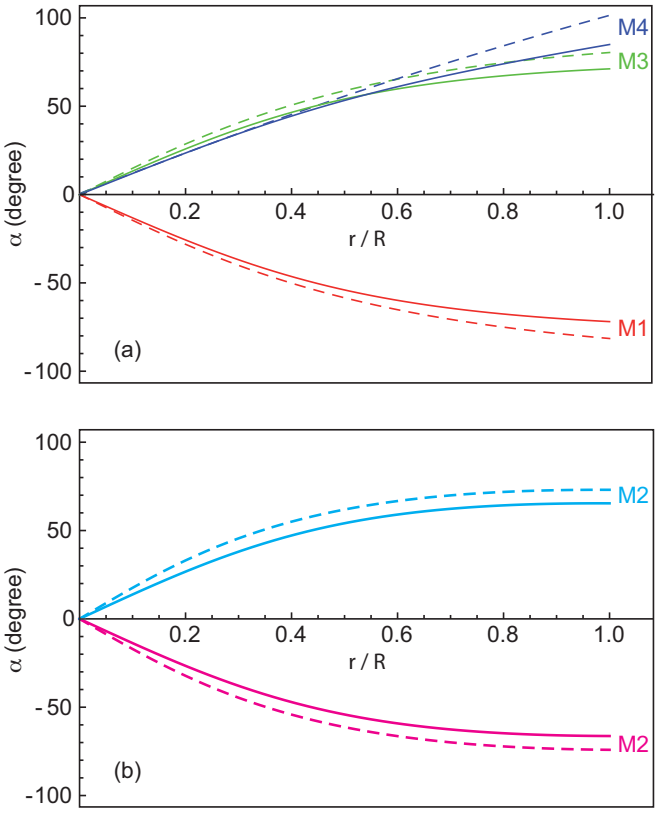

FIG. 16. Angle profiles $\alpha(r/R)$ calculated in the equatorial plane ($\xi = \pi/2$) with the generalized Williams model (solid lines) and the full numerics (dashed lines) for $R = 10\,\mu$m and the values of the pitch corresponding to mixtures M1-M4. (a) Red curves: $P = -145\,\mu$m (M1), green curves: $P = 167\,\mu$m (M3) and blue curves $P = 44\,\mu$m (M3) (b) Magenta and cyan curves: $P = -2000\,\mu$m (M2). The magenta lines correspond to a drop twisted left-handed (stable solution) and the cyan lines to a drop twisted right-handed (metastable solution). The two profiles are very similar except for the sign because the mixture is almost compensated. These two solutions are observed experimentally because their energies are very close.

We solved the differential equation (6) subjected to boundary conditions (7) and (8) with Mathematica by using a shooting method. Calculations were made by taking $K_{21} = 0.51$ and $K_{31} = 0.287$ which are the values found experimentally (see Fig. 7). Angle profiles $\alpha(r/R)$ in the equatorial plane $\xi = \pi/2$ are shown in Fig. 16. They have been calculated by taking $R = 10\,\mu$m and the values of the pitch corresponding to mixtures M1-M4. We recall that in this plane $r/R = \sin\eta/(1+\cos\eta)$. For the mixtures M1, M3 and M4 only the profiles corresponding to drops with a twist of the same sign as the spontaneous twist are shown (only these drops are observed) [graph (a)] while for the mixture M2, which is almost compensated, profiles corresponding to drops twisted in both directions are shown because the two types of drops are observed. For mixtures M1, M3 and M4, the drop energy in units of K_1R for a droplet of radius $R = 10\,\mu$m calculated from Eqs. (9)-(11) is equal to 9.49, 9.6 and 8.43, respectively. For mixture M2, the energies of left- and right-handed twisted drops are close, equal to 10.38 and 10.55, respectively. We emphasize that in these mixtures, the EC drops have always higher energy than the TB drops, as we can check by solving Eq. (6) with the boundary condition $\tau(\pi/2) = \text{sign}(P)\pi/2$ instead of Eq. (8). This calculation gives 12.21 in units of K_1R for the drop energy whatever the radius R, which is indeed greater than all the values given previously. Another interesting quantity is the twist angle $\alpha_S = \alpha(\pi/2)$ at the drop surface. We found that this angle varies almost linearly with the dimensionless quantity qR as we can see in Fig. 17, plotted by assuming $q > 0$. The best linear fit gives: $\alpha_s = 66.16\,\text{sign}(q) + 13.153qR$.

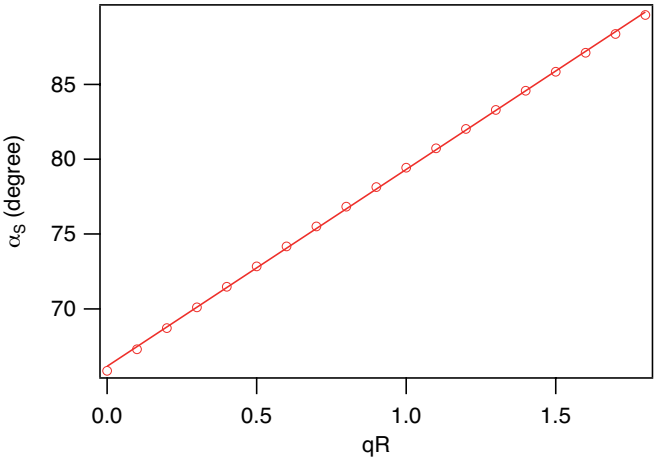

FIG. 17. Surface twist angle α_S calculated with the generalized Williams model as a function of the dimensionless product qR by assuming $q > 0$. The solid line is the best linear fit to the calculated points.

These variations of the twist angle explains the velocity changes between the drops of similar radius observed in the different mixtures. This point will be detailed in the last section once the Williams model and the twisted bipolar structure of the drops will be validated.

B. Full-vectorial 3D numerical calculation

The Williams calculation is not exact and is based on an ansatz for the director field according to which $\vec{n}$ has no $\vec{\eta}$ component and α does not depend on ξ. For this reason, we also calculated the director field using a completely vectorial 3D model to test the validity of this assumption. We used the numerical method described in [34], which is based on a Finite-Element discretization of the Frank elastic free-energy and a robust trust-region minimization algorithm. This method iteratively updates the director field solution by ensuring that the free energy is always decreased after each update, and always converges to a local minimum of the free energy.

We emphasize that the Williams model of the pre-

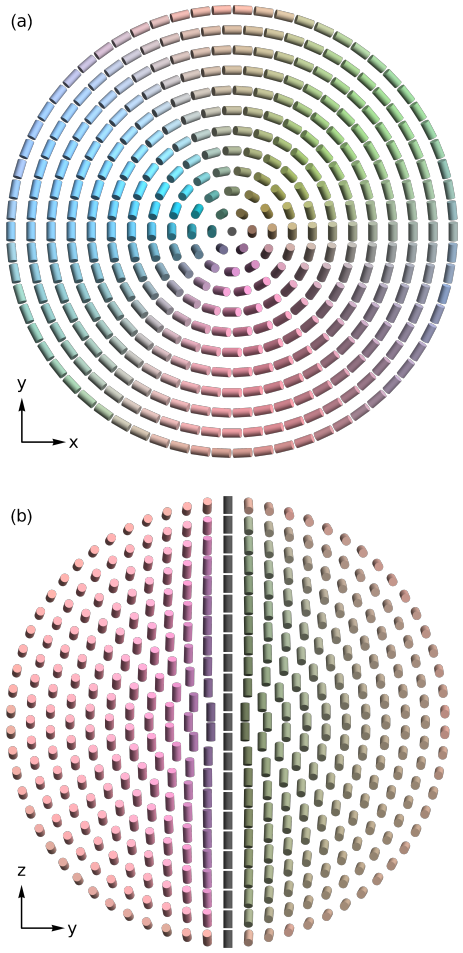

FIG. 18. Two cuts of the director field of a twisted bipolar droplet along the yz and xy planes, numerically calculated by taking $P/l_a = -145$ and $R/l_a = 5$. We used here a color scheme that associates in a quasi-unique manner a director with a CIELAB color, taking into account the $\vec{n} \to -\vec{n}$ symmetry [33]. Directors aligned with the polar axis are dark, while tilted directors span the red, green and blue colors of the hue circle when varying the azimuthal angle.

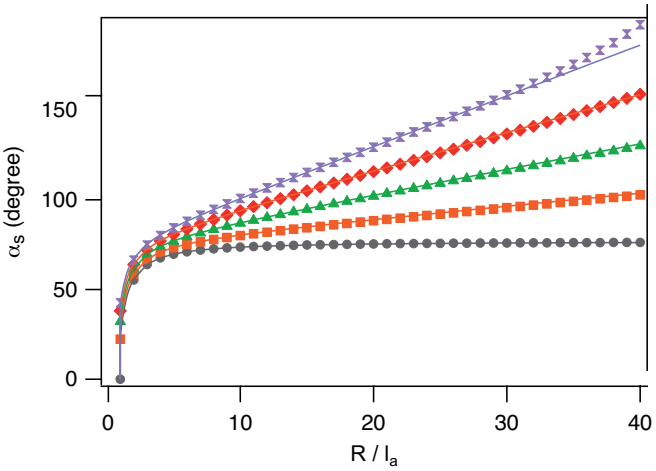

FIG. 19. Surface twist angle α_s as a function of the dimensionless parameters P/l_a and R/l_a. From top to bottom $P/l_a = 44, 58.7, 88, 176, \infty$. The solid lines have been calculated by using Eqs(12) and (13).

vious section assumes an infinitely strong planar anchoring at the surface of the droplet, which is valid if the droplet radius is much bigger than the anchoring penetration length $l_a \equiv K_1/W_a$ (with W_a the surface anchoring energy). This may not be a good approximation for our system since l_a is usually of the order of 1 µm for the nematic/isotropic interface of thermotropic liquid crystals [35], which is the same order of magnitude of the radius of the smallest droplets studied here. For this reason, we decided to simulate the director field of our droplets by assuming a finite anchoring strength and by rescaling all length scales (droplet radius R, cholesteric pitch P) by the anchoring length l_a. R/l_a and P/l_a are therefore the only adjustable parameters in our simulations, while all the other material constants were initialized with the values measured in Sec. II. Note that we did not measure the elastic constant K_4 associated with the Gauss (or saddle-splay) term $-(K_4/2)\nabla \cdot [\boldsymbol{n}\nabla \cdot \boldsymbol{n} + \boldsymbol{n} \times \nabla \times \boldsymbol{n}]$ in the free energy (using the definition of Ref. [34], for which the one-constant approximation is simply written as $K_1 = K_2 = K_3 = K_4 = K$). This constant is notoriously hard to obtain, which is why we arbitrarily used the Nehring-Saupe formula $K_4 = (K_1 + K_2)/2$ [36], but nevertheless checked that different values ranging from $K_1/2$ to $2K_2$ (the upper limit in the Ericksen inequalities) were not changing the twist angle α_s by more than 5 %. We also note that in the numerical simulation, the free energy density is always finite even near the (virtual) polar defects since the anchoring is finite and locally broken near these defects. An example of a calculated director field is shown in Fig. 18.

We first tried to determine if multiple metastable states could be found in our system by varying the initial director field in our simulations. We initialized the solution with a double twist cylinder director field with a given twist angle at the surface of the droplet, and found that the system always relaxed towards a twisted bipolar configure whatever the initial twist angle, except for very small droplets of radius R typically smaller than the anchoring length. This indicates that there exists a transition between bipolar and twisted-bipolar structures at small radius, with some metastability in the vicinity of the transition threshold in our numerical code. To confirm this point, we then calculated the surface twist angle α_s as a function of the dimensionless parameters P/l_a and R/l_a. The corresponding curves are shown in Fig. 19. When $q = 0$, we found that all droplets with $R < l_a$ are simply bipolar, i.e. associated with a surface angle $\alpha_s = 0$. Since all droplets are rotating in our experiments, we can therefore safely assume that the anchoring length is smaller than the smallest radius of our droplets, i.e. $l_a < 2\,\mu\text{m}$. In the following, we assume

$l_a \approx 1\,\mu m$, which is the right order of magnitude for the isotropic/nematic interface of common thermotropic liquid crystals [35].

Finally, we note that the data of Fig. 19 are well fitted in the range $R/l_a \in [2, 30]$ with an equation of the type:

$$\alpha_s = \sum_{i=0}^{2} (a_i \,\mathrm{sign}(q) + b_i q R)(l_a/R)^i \qquad (12)$$

with

$$\begin{cases} a_0 = 76.51^\circ \\ a_1 = -28.35^\circ \\ a_2 = -27.48^\circ \end{cases} \qquad \begin{cases} b_0 = 19.46^\circ \\ b_1 = -13.68^\circ \\ b_2 = 92.18^\circ \end{cases} \qquad (13)$$

as we can see in Fig. 19. Note that the data in this figure only include right-handed droplets with positive spontaneous twist. The sign(q) coefficient allows to extend, by symmetry, our results to left-handed droplets with negative spontaneous twist. Note that for the almost compensated mixture M2, metastable droplets which are right-handed despite the negative spontaneous twist can sometimes be observed (see Sec. III.B and Fig. 16), but our fit does not apply to such (rare) droplets.

This calculation shows that in the limit $l_a \to 0$ (strong anchoring) the angle α_s is approximately given by $76.51\,\mathrm{sign}(q) + 19.46qR$ while the Williams calculation gives $\alpha_s = 66.16\,\mathrm{sign}(q) + 13.153qR$. We conclude that the Williams calculation tends to underestimate the value of α_s by typically 15%, but is nevertheless in good qualitative agreement with the full numerical calculation despite the simplifications. This is also confirmed when looking at the curves $\alpha(r/R)$ calculated in the equatorial plane with the two models, which are very similar as shown in Fig. 16.

C. Drop image calculation and validation of the models

To determine if our experimental images indeed correspond to a twisted bipolar structure, we compared them to simulated optical micrographs based on the calculated director fields of Sec. IV.B. The optical simulations were performed using the open-source software *Nemaktis* that one of us developed [37]. We used the *BPM* simulation backend of this software; this backend is based on a generalized beam propagation method [38] allowing the accurate propagation of optical fields inside inhomogeneous birefringent media, including diffraction and walk-off effects in addition to phase propagation. A major advantage of this method is that the diffraction and walk-off operators at the core of the associated theory correctly model the deflection of light by spatially varying director fields, contrary to the well-known Jones method commonly used by researcher of the LC community. For comparison, we also calculated a few Jones images thanks to the *DTMM* backend of *Nemaktis*[39].

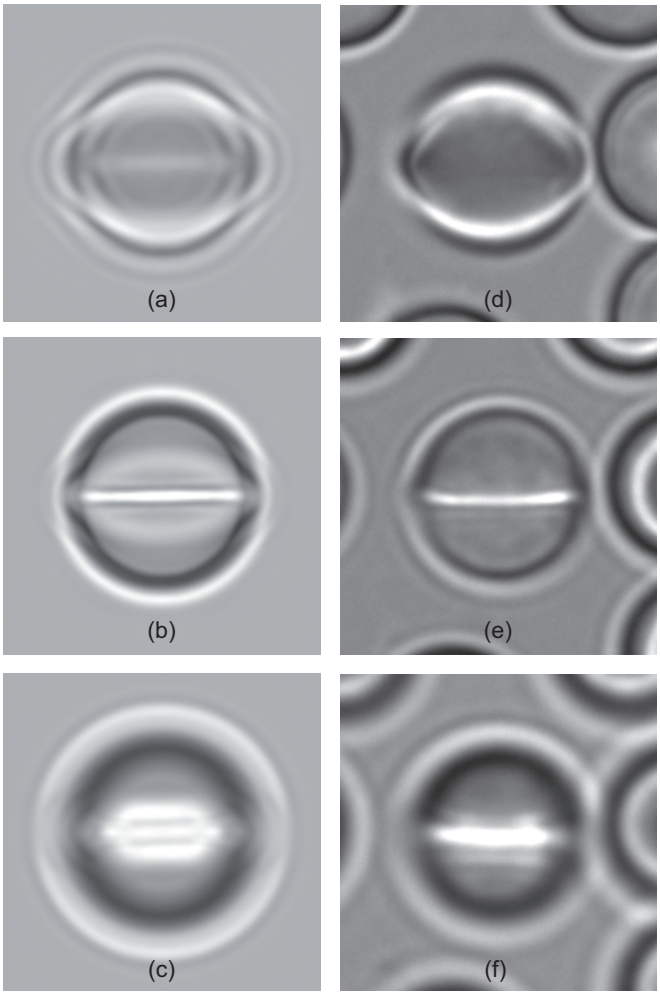

FIG. 20. Images in white light without polarizers of a horizontal drop of radius $R = 10\,\mu m$. (a-c) Grayscale images of the drop calculated with *Nemaktis* for three different focus adjustments. In (b) the focus is on the bright band ($z = 0$ by definition). In (a) $z = -15\,\mu m$ and in (c) $z = 15\,\mu m$. Calculations were performed by taking $P = -145\,\mu m$; (d-f) Experimental images observed in the same conditions in mixture M1.

Each optical simulation relies on the calculation of transmitted optical fields through a virtual sample consisting of two glass plates sandwiching the LC layer. We used the same sample parameters described in Sec. III and the refractive indices measured in Sec. II, while the radius and orientation of the droplet are varied between each simulation. We assumed the same cholesteric pitch as in mixture M1, i.e. $P = -145\,\mu m$. The Koehler illumination setup of a real microscope is approximated by using 37 incoming plane waves with wavevector uniformly distributed inside a cone of numerical aperture 0.05 (as in the experiments). The spectrum of the white lamp in our experiment was measured and evaluated at 11 wavelengths linearly spaced between 0.4 and $0.8\,\mu m$ in our simulations. The final monochrome images are obtained with a weighted average of all intensity images for

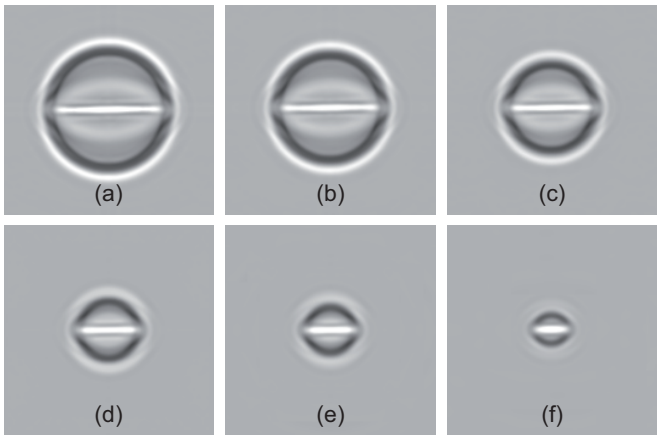

FIG. 21. Calculated grayscale images in white light without polarizers of horizontal drops of radii $R = 11.2, 10.2, 8.6, 6.1, 5.1$ and $3.5\,\mu$m when the focus is made on the bright band. Calculations were performed with *Nemaktis* by taking $P = -145\,\mu$m. These images are very similar to those observed experimentally in mixture M1 and shown in Fig. 9.

each incoming wavevector and wavelength, taking into account the amplitude point spread function of the microscope objective as well as the possible presence of a polarizer and/or analyzer along the path of light.

In Fig. 20, we show a comparison between experimental and simulated images of droplets with a horizontal polar axis when the sample is illuminated with natural light without polarizers. To demonstrate the effect of the focusing optics of the microscope, three different focus settings were compared, characterized by the z-position of the droplet with respect to a reference position where the droplet is well-focused, with the z-axis oriented from the microscope objective towards the sample. As visible in our simulations, a negative z-focus is associated with a bright elliptic ring near the droplet edge, a focused droplet is associated with a central bright line joining the two virtual surface polar defects, and a positive z-focus is associated with three central bright lines, in excellent agreement with the experimental images. We emphasize that the bright line visible in Fig. 20 is not due to a singular or non-singular defect with a sharp core, but to a lensing effect near the fully continuous core of the director field shown in Fig. 18. In fact, such an effect is very similar to the lensing effect that was recently observed when sending an in-sample-plane Gaussian beam near the continuous core of a toron or baby-skyrmion [40], which should come at no surprise since the mid-sample-plane of these structures is topologically equivalent to the xy-cut shown in Fig. 18. We also demonstrate in Fig. 21 that the central bright band is visible on all focused droplets whatever their sizes, in very good agreement with the experimental images of Fig. 9. Finally, we show in Fig. 22 a comparison between experimental and simulated images of focused droplets with a horizontal polar axis when the sample is illuminated with natural

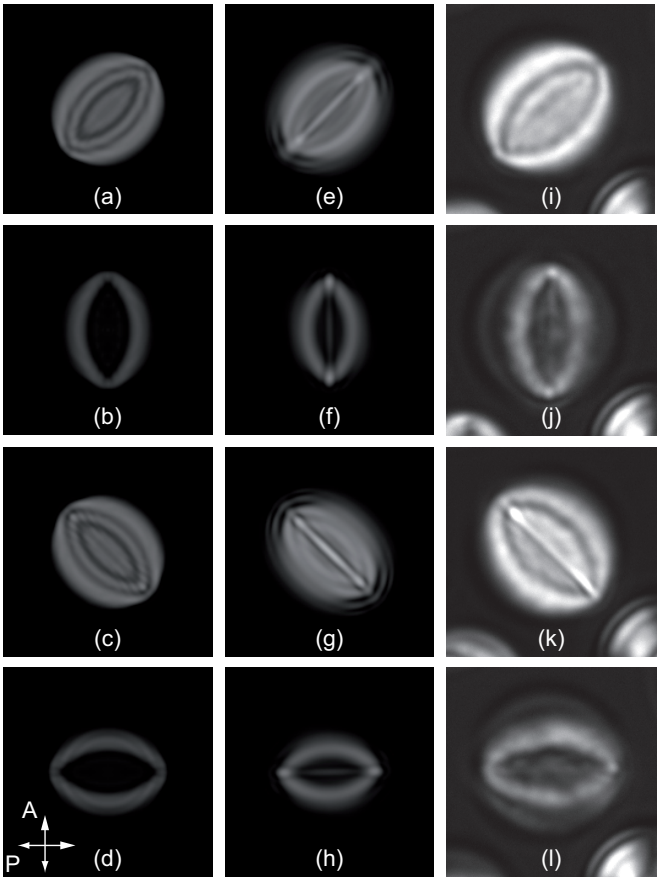

FIG. 22. Images in white light and between crossed polarizers of a horizontal drop of radius $R = 10\,\mu$m. (a-d) Grayscale images calculated with the Jones matrices. With this method, the images do not change with the focus; (e-h) Grayscale images calculated with *Nemaktis* when the focus is made on the bright band ($z = 0$). All calculations were made by taking $P = -145\,\mu$m. (i-l) Experimental images observed in the same conditions in mixture M1.

light between crossed polarizers. Again, the agreement between computed images and experiment is quite good, especially concerning the central bright band which is not reproduced by Jones calculations, shown for completeness on the left-most column of Fig. 22. Note that the bright band becomes invisible in the experimental configuration of Fig. 22i, but is visible in the associated numerical image (although dimmer than in Fig. 22g). We think this small disagreement is due to slightly wrong material constants in the simulations, which affect the twist profiles and optical constrast of the droplet. We checked that the bright band in Fig. 22e becomes even less visible by taking slightly smaller elastic constants (associated with a smaller twist angle), within the experimental accuracy of Sec. II.D (10 % for K_2/K_1 and 5 % for K_3/K_1).

In Fig. 23, we show a comparison similar to Fig. 20 for droplets with a polar axis aligned with the observation axis. The agreement is correct when the focus z is negative or zero, but not perfect when z is positive: al-

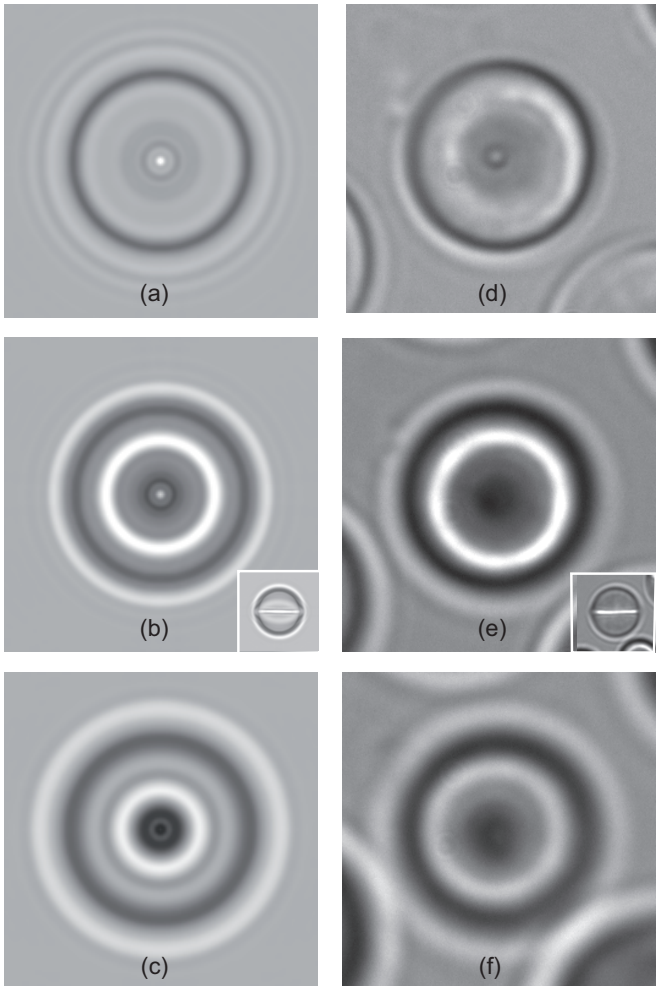

FIG. 23. Images in white light without polarizers of a vertical drop of radius $R = 10\,\mu$m. (a-c) Grayscale images of the drop calculated with *Nemaktis* for three different focuses. In (b) the focus is chosen in $z = 0$ as defined in Fig. 19. The inset shows a horizontal drop of same radius at the scale 1/4 for this focus. In (a) $z = -15\,\mu$m and in (c) $z = 15\,\mu$m. Calculations were performed by taking $P = -145\,\mu$m; (d-f) Experimental images observed in the same conditions in mixture M1. The inset in (e) shows a horizontal droplet of same radius at the scale 1/4 observed in the vicinity of the vertical drop with the same focus.

though two white concentric rings can be seen in both the experimental and simulated images, the intensity of the inner ring is much dimmer in the experimental image. This discrepancy can be due to slightly-off material constants, as above, or due to the fact that the droplet is slightly wetting one of the plate of the sample in our experiments, which is not taken into account in our simulations. We also show in Fig. 24 a comparison between experimental and simulated images of focused vertical droplets between crossed polarisers. Our simulation correctly reproduces the bright ring and dark cross of the experimental image, but again the agreement is not perfect at the center, which may be due to the same wetting

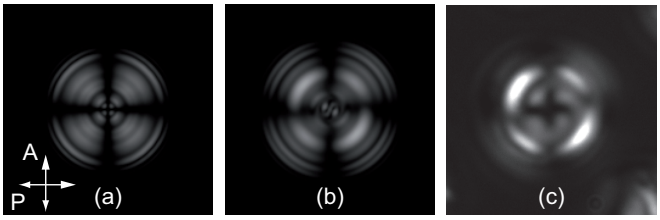

FIG. 24. Images in white light and between crossed polarizers of a vertical drop of radius $R = 10\,\mu$m. (a) Grayscale image calculated with the Jones matrices. With this method, the images do not change with the focus; (b) Grayscale image calculated with *Nemaktis* when focusing at $z = 0$. All calculations were made by taking $P = -145\,\mu$m. (c) Experimental image observed for this focus. The drop is the same as in Fig. 23 (mixture M1) .

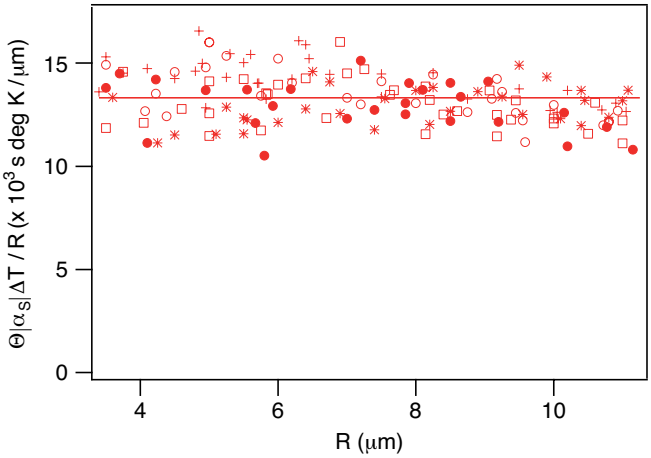

FIG. 25. Combination $\Theta\Delta T|\alpha_S|/R$ as a function of the drop radius R. The symbols for the experimental points are the same as in Fig. 14. This quantity is constant given the dispersion of the data.

effect described above. We note that the wetting of horizontal droplet does not cause a very visible discrepancy when comparing experiments and simulations, since the director field near the bottom/upper part of a horizontal droplet is much more uniform than near the same part of a vertical droplet, where a polar defect is present. Modeling this effect is out of the scope of this paper since it would necessitate a precise measurements of the surface tension potentials associated with both the surface polymercaptan layer and the cholesteric-isotropic interface.

V. A NEW SCALING LAW FOR THE LEHMANN ROTATION

Finally, we looked for a master curve that would account for all of our experimental results on the Lehmann effect. We have seen that the rotation period is proportional to R in mixture M2 which is almost compensated. In this mixture, the twist angle α_S is constant (or almost

constant). In the other mixtures, which are no longer compensated, we have seen that by increasing the twist angle α_S the period of rotation Θ decreases, suggesting that the latter is inversely proportional to α_S. As the period is also inversely proportional to the temperature gradient, we sought to see if the combination $\Theta\Delta T|\alpha_S|/R$ could allow us to gather all our experimental results on the same master curve. This is what we have verified by plotting this quantity for all the experimental points obtained with the mixtures M1-M4 as a function of the drop radius R. The final result is shown in Fig. 25. Except for the dispersion of the data, we see that all our points group together on the same master curve and that this quantity is almost constant. This scaling law completes our experimental results on the study of the Lehmann effect with twisted bipolar drops in strongly anisotropic materials such as the mixtures studied here or the chromonic liquid crystals studied previously [5].

VI. CONCLUSION

To summarize, we measured the optical indices and elastic constants of a mixture of CB7CB and 8CB, doped with with the surfactant 2-octadecoxypropanol, by introducing a convenient single-sample measurement technique for the elastic constants, which, to the best of our knowledge, was never used before. We note that the latter technique could be used in other systems where accurate measurements of all elastic constants of the nematic phase near a phase transition are needed. We experimentally characterized with optical microscopy the structural and dynamical properties of droplets of the same mixture subjected to a temperature gradient. By looking at the scaling of the Lehmann rotation period with respect to the droplet size in various mixtures with different amount of chiral dopant, we concluded that the previously conjectured escaped concentric structure was not possible in our system and that the droplets were likely adopting a more general twisted bipolar configuration. We confirmed this hypothesis by conducting director field and optical simulations of our experimental droplets using the measured material constants, and obtained a good agreement between experimental and simulated images of twisted bipolar droplets with a horizontal polar axis, and a reasonable agreement for the same study with a vertical polar axis. Finally, we used our numerical results to introduce an original scaling law for the Lehmann rotation period of twisted bipolar droplets with respect to the temperature gradient, twist angle and droplet size, and were able to collapse all our measurements on the same master curve.

An interesting point to further explore would be the stability of the polar axis of the twisted bipolar droplet studied here: our observations indeed suggest that the horizontal orientation of the polar axis is weakly unstable, contrary to the vertical orientation. This instability could be linked to the partial wetting of the droplet on the coldest plate of the sample. The coalescence process of droplets with vertical polar axes also deserves further investigation: as explained in this paper, we observed that the final orientation of the polar axis after coalescence is horizontal. Due to the Gauss-Bonnet theorem, defects with a total topological charge of -2 are necessarily created around the capillary bridge during the first stage of coalescence, such that the total charge of the new droplet is +2 when taking into the four +1 polar defects of the two coalescing droplets. It would be interesting to understand how these defects rearrange during the coalescence process depending on the value of the twist angle and would provide further insight into structural transformation of confined liquid crystal texture and defects [41, 42]. Finally, it would be interesting to explore the influence of an electric field on the Lehmann rotation of the drops, both in the AC and DC regimes where different effects are predicted from the theoretical models [43–45]. This could be all the more interesting in the DC regime as giant flexoelectric effects have been reported in CB7CB [46].

ACKNOWLEDGMENTS

The authors warmly thank J. Ignés-Mullol for his critical reading of the manuscript and useful comments and Dr W. Becker from Merck for the free sample of R811. K. S. K. is indebted to Dr. B. L. V. Prasad, Director, Centre for Nano and Soft Matter Sciences, India for supporting this collaborative work; also to the National Chemical Laboratory, India for the surfactant compound used in this study.

Appendix A: Fit procedure of the capacitance curves

The equations to solve to fit the capacitance curves like those shown in Fig. 6 are given in Ref. [47] and read:

$$\begin{cases} \dfrac{d}{2} = \displaystyle\int_{\theta_a}^{\theta_m} f_1(\theta, \theta_m, \phi'_m, \overline{C})\mathrm{d}\theta \\ \dfrac{\Phi}{2} = \displaystyle\int_{\theta_a}^{\theta_m} f_2(\theta, \theta_m, \phi'_m, \overline{C})\mathrm{d}\theta \\ \dfrac{V}{2} = \dfrac{D}{\varepsilon_0\varepsilon_\parallel}\displaystyle\int_{\theta_a}^{\theta_m} f_3(\theta, \theta_m, \phi'_m, \overline{C})\mathrm{d}\theta \end{cases} \tag{A1}$$

The first two come from the bulk torque equation and the third one comes from the Maxwell equation for the electric field. In these equations, $\overline{C} = C/C_\perp$ is the capacitance normalized with the capacitance $C_\perp = \frac{\varepsilon_0\varepsilon_\perp S}{d}$ (with S the electrode surface area). Functions f_1, f_2 and f_3 are given by:

$$\begin{cases} f_1(\theta,\dots) = \sqrt{\dfrac{1-\gamma_1\sin^2\theta}{(\cos^2\theta-\cos^2\theta_m)g(\theta,\dots)}} \\ f_2(\theta,\dots) = \dfrac{K_3\cos^2\theta_m(1-\gamma_2\cos^2\theta_m)+K_2q(\cos^2\theta-\cos^2\theta_m)}{K_3\cos^2\theta(1-\gamma_2\cos^2\theta)}\, f_1(\theta,\dots) \\ f_3(\theta,\dots) = \dfrac{1}{1-\alpha\cos^2\theta}\, f_1(\theta,\dots) \end{cases} \tag{A2}$$

where

$$g(\theta,\theta_m,\phi'_m,\overline{C}) = D^2\frac{\alpha}{K_3\varepsilon_0\varepsilon_\parallel}\frac{1}{(1-\alpha\cos^2\theta)(1-\alpha\cos^2\theta_m)} + \frac{\cos^2\theta_m(1-\gamma_2\cos^2\theta_m)(1-\gamma_2(\cos^2\theta+\cos^2\theta_m))}{\cos^2\theta(1-\gamma_2\cos^2\theta)}{\phi'_m}^2 - \frac{2qK_2\cos^2\theta_m(1-\gamma_2\cos^2\theta_m)}{K_3\cos^2\theta(1-\gamma_2\cos^2\theta)}\phi'_m - \frac{q^2K_2^2(\cos^2\theta-\cos^2\theta_m)}{K_3^2\cos^2\theta(1-\gamma_2\cos^2\theta)} \tag{A3}$$

Angles θ and ϕ are the polar and azimuthal angles, with $\theta=\theta_a$ and $\phi=0$ on the bottom electrode at $z=0$ and $\theta=\theta_a$ and $\phi=\Phi$ on the top electrode at $z=d$, $\theta_m=\theta(d/2)$, $\phi'_m=(\mathrm{d}\phi/\mathrm{d}z)(d/2)$, $q=2\pi/P$ is the measured equilibrium twist, $\gamma_1=1-K_1/K_3$, $\gamma_2=1-K_2/K_3$, $\alpha=\varepsilon_a/\varepsilon_\parallel$ and $D=CV/S=\varepsilon_0\varepsilon_\perp(V/d)\overline{C}$ is the electric displacement, constant within the sample thickness in the dielectric regime.

The fit procedure was as follows.

First, we determined the two dielectric constants. This measurement was performed when the sample was well oriented and not twisted. Constant $\epsilon_\perp$ was obtained by extrapolating to 0 the capacitance curve measured below the onset of Fredericksz instability. This gave $C_\perp$ from which $\epsilon_\perp$ was deduced by dividing by the capacitance C_0 of the empty cell. Constant $\epsilon_\parallel$ was obtained by measuring the capacitance curve between 3 V and 20 V. In this voltage range, the curve $C(1/V)$ was perfectly linear in all our experiments. Capacitance $C_\parallel$ was obtained by extrapolating this curve to 0 from which $\epsilon_\parallel$ was deduced by dividing by C_0.

Second, we fitted the capacitance curve measured by increasing the voltage when the director field was not twisted. In practice, we chose to work with a parallel planar sample. In a previous paper [23], we have shown that, with a very good approximation, the measured curve is the same as that which would be measured with a zero anchoring angle θ_0. This remarkable result therefore allowed us to fit our capacity curves with the previous equations, only valid for symmetric boundary conditions, by taking $\theta_a=0$. To solve Eqs. (A1) with unknowns θ_m, ϕ'_m and $\overline{C}$, we used Mathematica and proceeded by successive approximations by taking $\theta_0=0.1^\circ$ for numerical reasons (this does not change the final result). In practice K_1 was obtained by adjusting the threshold of instability and K_3 by fitting at best the shape of the capacitance curve above the onset of instability.

Third, we fitted the capacitance curve measured by decreasing the voltage after the sample has been twisted by π at large voltage. In that case, the equations were solved by taking $\Phi=\pi$ when q was positive and $\Phi=-\pi$ when q was negative. The fit parameters were the anchoring angle θ_a and the twist constant K_2 by taking the values of K_1, K_3 and P found previously. We emphasize that good fits could only be obtained by taking into account the spontaneous twist of the phase, which confirmed our mixture C15 was chiral. In practice K_2 mainly determined the onset of instability, while θ made it possible to adjust the shape of the curve in the vicinity of the critical voltage. Good fits were generally obtained by taking $\theta_a=2^\circ$.

With this procedure, it was possible to measure all the constants with the same sample, a crucial point when measurements are made near the melting point.

[1] O. Lehmann, Structur, System und magnetisches Verhalten flüssiger Krystalle und deren Mischbarkeit mit festen, Ann. Phys. **307**, 649 (1900).

[2] P. Oswald and A. Dequidt, Measurement of the Continuous Lehmann Rotation of Cholesteric Droplets Subjected to a Temperature Gradient, Phys. Rev. Lett. **100**, 217802 (2008).

[3] F. Ito, J. Yoshioka, and Y. Tabe, Heat-driven rotation in cholesteric droplets with a double twisted structure, J. Phys. Soc. Jpn **85**, 14601 (2016).

[4] T. Yamamoto, M. Kuroda, and M. Sano, Three-dimensional analysis of thermo-mechanically rotating cholesteric liquid crystal droplets under a temperature gradient, Europhys. Lett. **109**, 46001 (2015).

[5] J. Ignés-Mullol, G. Poy, and P. Oswald, Continuous rotation of achiral nematic liquid crystal droplets driven by heat flux, Phys. Rev. Lett. **117**, 057801 (2016).

[6] R. Zhang, A. Mozaffari, and J. J. de Pablo, Autonomous materials systems from active liquid crystals, Nat. Rev. Mater. **6**, 437 (2021).

[7] P. Oswald, A. Dequidt, and G. Poy, Lehmann effect in nematic and cholesteric liquid crystals: a review, Liq. Cryst. Rev. **85**, 142 (2019).

[8] C. Meyer, G. R. Luckhurst, and I. Dozov, Flexoelectrically driven electroclinic effect in the twist-bend nematic phase of achiral molecules with bent shapes, Phys. Rev.

Lett. **111**, 067801 (2013).
[9] P. S. Drzaic, A case of mistaken identity: spontaneous formation of twisted bipolar droplets from achiral nematic materials, Liq. Cryst. **26**, 623 (1999).
[10] J. Ignés-Mullol, M. Mora, B. Martínez-Prat, I. Vélez-Cerón, R. S. Herrera, and F. Sagués, Stable and metastable patterns in chromonic nematic liquid crystal droplets forced with static and dynamic magnetic fields, Crystals **10**, 138 (2020).
[11] K. S. Krishnamurthy, D. S. Shankar Rao, S. Sharma, and C. V. Yelamaggad, Structure, stability, and electro-optic features of nematic drops in 1", 7"-bis (4-cyanobiphenyl-4'-yl) heptane–surfactant binary systems, Phys. Rev. E **105**, 024709 (2022).
[12] A. Jákli, O. D. Lavrentovich, and J. V. Selinger, Physics of liquid crystals of bent-shaped molecules, Rev. Mod. Phys. **90**, 045004 (2018).
[13] A. Aouini, M. Nobili, E. Chauveau, P. Dieudonne-George, G. Dameme, D. Stoenescu, I. Dozov, and C. Blanc, Chemical-physical characterization of a binary mixture of a twist bend nematic liquid crystal with a smectogen, Crystals **10**, 1110 (2020).
[14] P. Oswald, Surface-field induced heliconical instability in the cholesteric phase of a mixture of a flexible dimer (CB7CB) and a rod-like molecule (8CB), Phys. Rev. E **105**, 024704 (2022).
[15] J. Kędzierski, Z. Raszewski, M. Kojdecki, E. Kruszelnicki-Nowinowski, P. Perkowski, W. Piecek, E. Miszczyk, J. Zieliński, P. Morawiak, and K. Ogrodnik, Determination of ordinary and extraordinary refractive indices of nematic liquid crystals by using wedge cells, Opto-Electron. Rev. **18**, 214 (2010).
[16] H. Ozbek, S. Ustunel, E. Kutlu, and M. C. Cetinkaya, A simple method to determine high-accuracy refractive indices of liquid crystals and the temperature behavior of the related optical parameters via high-resolution birefringence data, J. Mol. Liq. **199**, 275 (2014).
[17] P. Oswald and P. Pieranski, *Nematic and Cholesteric Liquid Crystals: Concepts and Physical Properties Illustrated by Experiments* (Taylor & Francis, CRC press, Boca Raton, 2005).
[18] H. L. Ong, Origin and characteristics of the optical properties of general twisted nematic liquid-crystal displays, J. Appl. Phys. **64**, 614 (1988).
[19] I.-C. Khoo and S.-T. Wu, *Optics and nonlinear optics of liquid crystals*, Vol. 1 (World Scientific, 1993) p. 126.
[20] N. A. Kasian, L. N. Lisetski, and I. A. Gvozdovskyy, Twist-bend nematics and heliconical cholesterics: a physico-chemical analysis of phase transitions and related specific properties, Liq. Cryst. **49**, 142 (2022).
[21] P. Oswald and A. Dequidt, Heliconical-fluctuation-induced compensation point in the diluted cholesteric phase of mixtures containing the flexible dimer CB7CB, Phys. Rev. E **105**, 024707 (2022).
[22] I. Dozov and P. Martinot-Lagarde, First-order breaking transition of tilted nematic anchoring, Phys. Rev. E **58**, 7442 (1998).
[23] P. Oswald and J. Colombier, On the measurement of the bend elastic constant in nematic liquid crystals close to the nematic-to-SmA and the nematic-to-N_{TB} phase transitions, Liq. Cryst. **48**, 1608 (2021).
[24] P. Martinot-Lagarde, H. Dreyfus-Lambez, and I. Dozov, Biaxial melting of the nematic order under a strong electric field, Phys. Rev. E **67**, 051710 (2003).
[25] P. Oswald, Easy axis memorization with active control of the azimuthal anchoring energy in nematic liquid crystals, Europhys. Lett.) **107**, 26003 (2014).
[26] See Supplemental Material SM1 at [URL will be inserted by publisher] for a movie of coalescing droplets.
[27] J. Jiang and D.-K. Yang, Bipolar to toroidal configuration transition in liquid crystal droplets, Liq. Cryst. **45**, 102 (2018).
[28] J. Wu, H. Ma, S. Chen, X. Zhou, and Z. Zhang, Study on concentric configuration of nematic liquid crystal droplet by landau-de gennes theory, Liq. Cryst. **47**, 1698 (2020).
[29] See Supplemental Material SM2 at [URL will be inserted by publisher] for a movie of a spontaneously reorienting droplet.
[30] See Supplemental Material SM3 at [URL will be inserted by publisher] for a movie of droplets of mixture M2 rotating in opposite directions. Note that a x2 optical block was used in the microscope for this movie, which allowed us to get a better magnification at the expense of optical quality.
[31] P. Oswald, G. Poy, and A. Dequidt, Lehmann rotation of twisted bipolar cholesteric droplets: role of Leslie, Akopyan and Zel?dovich thermomechanical coupling terms of nematodynamics, Liq. Cryst. **44**, 969 (2017).
[32] R. D. Williams, Two transitions in tangentially anchored nematic droplets, J. Phys. A: Math. Gen. **19**, 3211 (1986).
[33] G. Poy, A. J. Hess, A. K. Seracuse, M. Paul, S. Žumer, and I. I. Smalyukh, Interaction and co-assembly of optical and topological solitons, Nat. Photonics 10.1038/s41566-022-01002-1 (2022).
[34] G. Poy, F. Bunel, and P. Oswald, Role of anchoring energy on the texture of cholesteric droplets: Finite-element simulations and experiments, Phys. Rev. E **96**, 012705 (2017).
[35] S. Faetti and V. Palleschi, Nematic-isotropic interface of some members of the homologous series of 4-cyano-4'-(n-alkyl) biphenyl liquid crystals, Phys. Rev. A **30**, 3241 (1984).
[36] J. Nehring and A. Saupe, On the elastic theory of uniaxial liquid crystals, The Journal of Chemical Physics **54**, 337 (1971).
[37] G. Poy and A. Petelin, Nemaktis v1.4.4, https://nemaktis.readthedocs.io/en/latest/ (2022).
[38] G. Poy and S. Žumer, Physics-based multistep beam propagation in inhomogeneous birefringent media, Opt. Express **28**, 24327 (2020).
[39] We note that this backend corresponds to a simple interface to the full-fledged python library *dtmm* [48], which also supports advanced simulation such as reflection microscopy with full diffractive effects. This library provides the same kind of accurate field propagation than our *BPM* backend, the difference being than it relies on a Fourier iterative procedure whereas our beam propagation method use a real-space non-iterative procedure. The degree of accuracy of *dtmm* is controlled by a "diffraction" parameter, with a value of 0 associated with the Jones method and higher values associated with more accurate simulation with difractive effects.
[40] A. J. Hess, G. Poy, J.-S. B. Tai, S. Žumer, and I. I. Smalyukh, Control of light by topological solitons in soft chiral birefringent media, Phys. Rev. X **10**, 031042 (2020).
[41] T. Lopez-Leon, M. A. Bates, and A. Fernandez-Nieves,

Defect coalescence in spherical nematic shells, Phys. Rev. E **86**, 030702 (2012).

[42] P.-X. Wang and M. J. MacLachlan, Liquid crystalline tactoids: ordered structure, defective coalescence and evolution in confined geometries, Philos. Trans. Royal Soc. A **376**, 20170042 (2018).

[43] O. S. Tarasov, A. P. Krekhov, and L. Kramer, Rotation of cholesteric drops under dc electric field. preprint, This paper was never published after the death of L. Kramer (2003).

[44] O. A. Skaldin, O. S. Tarasov, Y. I. Timirov, and E. R. Basyrova, Mechanisms of rotational dynamics of chiral liquid crystal droplets in an electric field, J. Exp. Theo. Phys. **126**, 255 (2018).

[45] P. Oswald, Role of an oscillatory electric field on the Lehmann rotation of cholesteric droplets, Eur. Phys. J. E **43**, 1 (2020).

[46] A. Varanytsia and L.-C. Chien, Giant flexoelectro-optic effect with liquid crystal dimer CB7CB, Sci. Rep. **7**, 1 (2017).

[47] H. A. Van Sprang and P. A. Breddels, Numerical calculations of director patterns in highly twisted nematic configurations with nonzero pretilt angles, J. Appl. Phys. **60**, 968 (1986).

[48] A. Petelin, dtmm v0.6.1, https://github.com/ijscomplexmatter/dtmm (2022).